Particle localization with DPTV and sizing with IPI using a forward model and optimization

IOP Publishing Meas. Sci. Technol. 37 (2026) 025201 https://doi.org/10.1088/1361-6501/ae2641

Measurement Science and Technology

PAPER

Particle localization with DPTV and sizing with IPI using a forward model and optimization

Christian Sax[1,2], **Roland Griesmaier**[2] and **Jochen Kriegseis**[1,*]

[1] Institute of Fluids Mechanics (ISTM),Karlsruhe Institute of Technology (KIT), Kaiserstraße 10, 76131 Karlsruhe, Germany
[2] Institute of Applied and Numerical Mathematics (IANM), Karlsruhe Institute of Technology (KIT), Englerstraße 2, 76131 Karlsruhe, Germany
[*] Author to whom any correspondence should be addressed.

E-mail: jochen.kriegseis@kit.edu

Keywords: interferometric particle imaging, 3D particle localization, bubbles, droplets, inverse problem, disperse two-phase flow

OPEN ACCESS

RECEIVED
4 June 2025

REVISED
8 October 2025

ACCEPTED FOR PUBLICATION
1 December 2025

PUBLISHED
26 December 2025

Abstract

An inverse problem (IP) approach is proposed to simultaneously determine the three-dimensional position and size of bubbles or droplets in a two phase flow from a single camera image. The method is based on interferometric particle imaging (IPI) and defocusing particle tracking velocimetry. A forward model (FM) is introduced that integrates a scattering model based on geometrical optics and the Lorentz–Mie theory, along with a wave propagation model based on the Huygens–Fresnel principle to simulate particle images. Using bounding boxes from object detection methods as initialization, the InvP approach approximates the position and diameter of each particle in the image. The performance of the presented approach is evaluated on the grounds of the data achieved by Sax *et al* (2025 *Phys. Rev. Appl.* **24** 044083): As key aspects it achieves subpixel accuracy in position determination, exceeds the diameter accuracy of current FFT-based benchmarks on real data and furthermore achieves sub-micrometre precision in diameter resolution, even for three-dimensionally distributed particles. The InvP approach achieves a decoupling of the diameter estimation from the out-of-plane position estimation, thus avoiding error propagation from one to the other, which significantly increases the sizing accuracy. The incorporated FM accounts for aliasing effects in the interference pattern, effectively increasing the measurable volume both closer to and further from the focal plane. This improvement qualifies the approach to measure closer to the focal plane, which in turn allows to obtain images with higher signal-to-noise ratio (SNR). The InvP approach is capable of handling significantly lower SNRs compared to commonly applied algorithms and noise levels at which detection algorithms typically fail, presenting significant potential for single optical access IPI in side- and backscatter regions where low SNR usually necessitates sophisticated data processing methods. Notably, the InvP approach is largely unaffected by particle image overlaps, addressing another major challenge in single-camera particle tracking and sizing at high source densities in a given field of view.

1. Introduction

Dispersed two-phase flows, including bubble flows, mist flows and sprays, are central to many scientific and engineering problems. The three-dimensional tracking and sizing of small dispersed particles, such as droplets and bubbles, provide essential information and are therefore at the centre of experimental investigations [1–4]. Many applications require single camera techniques to determine the three dimensional position and size of particles due to limited optical access or other constraints. Single camera techniques for the three dimensional position reconstruction include astigmatism particle tracking velocimetry (APTV) [5], defocusing PTV (DPTV) [6, 7] and holographic PTV [8]. The first two techniques use the amount of defocusing of the particle images (PI), i.e. the size (DPTV) or aspect ratio (APTV) of the PI, to determine the out-of-plane position (z-position). Digital in-line holography uses numerical

refocusing in different z-planes to find the matching z-position. However, for all these techniques, the out-of-plane uncertainty is typically an order of magnitude larger than the in-plane accuracy (for the x, y position)[9]. For DPTV and APTV, PI overlaps add an additional challenge to determine the z-position, as the edges of the PI are less clearly identifiable, and therefore, the size or aspect ratio is more difficult to determine. Recent advances in particle detection using convolutional neural networks (CNN) [10, 11] have improved the detection of PIs in the presence of PI overlap in APTV [12, 13] and in DPTV [14–16]. Another issue in DPTV is the intensity loss with increased defocusing, which renders PIs far away from the focal plane difficult to detect and evaluate. This issue presents an effective limit to the depth of the measurement volume in DPTV.

While the position of particles is essential for tracking, their size is often of additional interest. Prominent single camera techniques for particle sizing in comparatively large fields of view are shadowgraphy, digital in-line holography and interferometric particle imaging (IPI) [1, 2, 17]. In shadowgraphy and holography, the size of the particles is determined directly from the size of the (refocused) PIs and the magnification. Interpolation techniques can be used in in-focus techniques to achieve subpixel accuracy; however, this process is limited by the resolution of the focused PI. In IPI, on the other hand, the particle size is reconstructed based on the interference pattern that appears when the particle is imaged out-of-focus. The particle size then can be retrieved from either the number of fringes in the pattern or from the fringe frequency, with the latter method having turned out to be the more accurate one [2, 18, 19]. IPI offers the advantage of low uncertainty in size determination compared to in-focus techniques due to the higher accuracy of the frequency measurement compared to the sizing of in-focus PIs.

The interpretation of the interference pattern in IPI requires the distance of the particle to the camera to be known. As a consequence, IPI is predominantly used with light sheets as the z-position is then known, which, however, limits IPI to two dimensionally distributed particles, rather than three 3D volumes, This limitation presents a major drawback of IPI to holography, that allows for the sizing of particles in 3D volumes. More recently, some approaches have extended IPI to the sizing of three-dimensionally distributed particles using an APTV approach [20, 21]. The expansion of IPI to 3D volumes presents a major challenge as an error in the z-position propagates into the diameter estimation, effectively diminishing the accuracy advantage of IPI over in-focus techniques. An additional problem is again PI overlap, as it causes irregular and super-positioned interference patterns, which in turn make the determination of the particle size more difficult and often lead to erroneous particle sizes. PI overlaps in IPI are usually avoided by optical compression [22]. However, this only works if the particles are at a certain distance from the focal plane, and is therefore not feasible for volume measurements. A further challenge is the measurement of particles that are very large compared to their amount of defocusing. The fringe distance becomes so small for such large particles, that aliasing occurs. This effect cannot be captured with frequency and fringe counting methods, so that either method cannot be employed for such particles. Aliasing of the fringes presents an upper limit to the particle sizes that can be measured with IPI [23].

For digital in-line holography, the accuracy of both size and z-position determination have been improved by more than an order of magnitude by an inverse problem (IP) approach [24–26]. In this type of approach, a forward model (FM) simulates the PIs according to certain particle parameters and the resulting synthetic image is being compared to the observed image. The match between simulated and observed image is quantified by a mismatch functional, which is minimized in the process of finding the unknown particle parameters.

In continuation of efforts for InvP approaches for holography and the development of FMs for IPI [27], the present work explores an InvP approach to IPI and DPTV. The DPTV approach is chosen to enable the measurement of three-dimensionally distributed particles. The IPI approach is chosen due to its higher theoretical limits on accuracy, compared to in-focus techniques for particle sizing. The InvP approach to DPTV and IPI addresses the following main issues: First, the lower out-of-plane accuracy of DPTV is addressed. Decoupling of the size and z-position estimation prevent error propagation and allows for IPI to be expanded to 3D volumes without loss of sizing accuracy. The issue of PI overlap common to DPTV and IPI is addressed, as the FM can account for superpositions of interference patterns and PIs. Lastly, the aliasing issue is addressed, as the FM can also account for aliasing, in contrast to conventional evaluation methods in IPI.

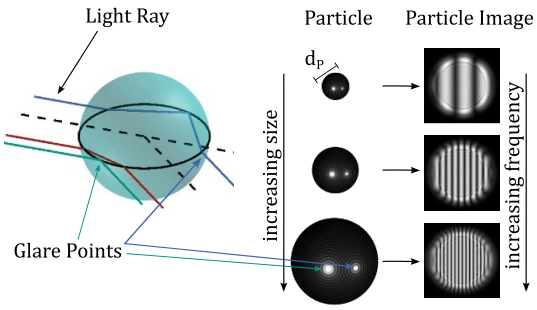

Figure 1. Scattering of monochromatic light at a bubble ($m = 1/1.333$) as modelled by the GO approach. The different colours of the light rays represent the different scattering orders $p = 0$ (●), $p = 1$ (●), $p = 2$ (●). The GPs are visualized on the sphere and the corresponding PI is shown. The black particles show the actual distribution of light intensity over the particle as computed from the Lorentz–Mie theory [28]. The frequency of the pattern in the PI increases with the size of the particle.

2. Theory and fundamentals

2.1. IPI

IPI was originally introduced as interferometric laser imaging for droplet sizing [1, 17] and later extended to bubbles [2, 18] where it was renamed as IPI. The method is used to size transparent spherical particles with a refractive index n_1 that differs from the refractive index n_2 of its surrounding medium. The relative refractive index $m = n_1/n_2$ is used to describe the relationship between these refractive indices. In IPI a particle is illuminated with coherent, monochromatic and polarized light, i.e. a laser. The light scattered by the particle can be seen as glare points (GP) [28, 29] on the particle surface when viewed from the scattering angle θ. This process is best visualized using the geometric optics (GO) model, viewing parallel rays of light being either reflected (scattering order $p = 0$) or refracted (order $p > 0$) at the particle surface. The scattering order p refers to the number of cords the light has travelled inside the particle. While light is scattered in all directions, when interacting with a particle, only light that is scattered in direction (approx.) parallel to the optical axis of the camera, eventually reaches the camera chip. The angle between the laser illuminating the particle and the optical axis of the camera angle is the scattering angle θ.

As these are the only rays observed by the camera, all other rays are discarded in this model. This process depends on the relative refractive index m and the scattering angle θ [29]. The light scattered by the particle forms an interference pattern on the camera chip. Since most of the light intensity emitted from the particle is contained in the GPs, the model can be simplified to the light emitted from the GPs only, as can be seen by the bright spots on the spheres in figure 1. The frequency of the interference pattern is a function of the distance between the GPs $\Delta_{\mathrm{GP}}^{\mathrm{phys}}$ and therefore of the particle size, since the relative position of the GPs on the particle depends on m and θ but not on the particle size. In IPI, two types of particles are distinguished: droplets ($m > 1$) and bubbles ($m < 1$), as the scattering process differs due to the different refraction at the particle surface as described by Snell's law. For most scattering angles, the interference pattern is the result of two GPs, but third GPs can also cause patterns with superimposed frequencies [23, 30].

Different formulations exist to describe the relationship between the particle diameter d_P and the frequency F of the interference pattern, but the most general description was provided by Shen *et al* [27] as

$$\frac{1}{F} = \frac{|\lambda B_{\mathrm{tot}}|}{\Delta_{\mathrm{GP}}^{\mathrm{phys}}}, \tag{1}$$

which is valid for any paraxial optical system and scattering angle. The wavelength of light in vacuum is described by λ and the distance between the GPs is $\Delta_{\mathrm{GP}}^{\mathrm{phys}}$. A scattering model is required to make the connection between the GP spacing $\Delta_{\mathrm{GP}(\theta)}^{\mathrm{phys}}$ and the particle diameter for different scattering angles [23]. The GO model can be used as the simplest model to describe the GP position [29] and is sufficiently accurate for particle sizes relevant to IPI. The GO model provides the relative position $w_i \in [-1, 1]$ of a GP of order $p = i$ on the particle surface, so that

$$\Delta_{\mathrm{GP}(\theta)}^{\mathrm{phys}} = \frac{d_P}{2}|w_i - w_j| = \frac{d_P}{2}\Delta_{\mathrm{GP}(\theta)}. \tag{2}$$

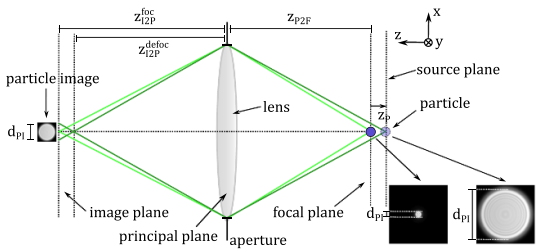

Figure 2. Working Principle of DPTV visualized. As the particle moves away from the focal plane the particle image visible on the image plane becomes defocused and the diameter of the PI increases.

The GP distance $\Delta^{\text{phys}}_{\text{GP}(\theta)}$ can be derived from its dimensionless form $\Delta_{\text{GP}(\theta)} = |w_i - w_j|$. The term B_{tot} describes the amount of defocus and is derived from the ray transfer matrix (RTM), which characterizes the paraxial optical system [31, 32]. The RTM describes the change of the distance to the optical axis x_{ray} and angle ϕ_{ray} of an arbitrary ray relative to the optical axis as it travels along the z direction. It has the form

$$\begin{pmatrix} x_{\text{ray},z_1} \\ \phi_{\text{ray},z_1} \end{pmatrix} = \underbrace{\begin{bmatrix} A_{\text{tot}} & B_{\text{tot}} \\ C_{\text{tot}} & D_{\text{tot}} \end{bmatrix}}_{:=M_{\text{tot}}} \begin{pmatrix} x_{\text{ray},z_0} \\ \phi_{\text{ray},z_0} \end{pmatrix} \tag{3}$$

Equation (1) requires the amount of defocus B_{tot} of the PI to be known, which in turn requires the position of the particle along the optical axis (i.e. the z-position) to be known. While the z-position is usually known when IPI is performed with a light sheet, three-dimensionally distributed particles require *a priori* determination of the z-position. For most optical systems, i.e. optically homogeneous surrounding medium n_2, B_{tot} changes linearly with the z-position of the particle, so an error in the z-position propagates linearly into the diameter determination.

2.2. Defocusing particle tracking velocimetry (DPTV)

DPTV is a popular single camera technique that is used to determine the three dimensional position of particles. Since IPI and DPTV require the same setup, the techniques can be combined [33] and the defocusing approach can be used to determine the z-position of the particle from the diameter of the PI.

In DPTV the z-position is determined from the amount of defocusing of the PI i.e. the PI diameter d_{PI} [34]. The relationship of the PI diameter and the distance of the particle to the focal plane becomes linear with sufficient distance to the focal plane [7]. Therefore, at sufficient distance from the focal plane, the relationship between d_{PI} and z_{P} can be described by a GO model [27] via

$$d_{\text{PI}} = D_{\text{a}} \frac{|z_{\text{I2P}}^{\text{foc}} - z_{\text{I2P}}^{\text{defoc}}|}{z_{\text{I2P}}^{\text{foc}}} \tag{4}$$

where $z_{\text{I2P}}^{\text{foc}}$ is the distance from the image plane to the principal plane (I2P), see figure 2. The distance between the principal plane and the focal plane (P2F) is accordingly labelled as z_{P2F}. In the present context, the image plane is the position of the camera chip. While the position of the principal plane (location of the imaging lens) and the focal plane are usually unknown, they can be calculated from the magnification and the thin lens equation

$$\frac{1}{z_{\text{I2P}}^{\text{foc}}} + \frac{1}{z_{\text{P2F}}} = \frac{1}{f_{\text{lens}}} \tag{5}$$

using a calibration target [23], with f_{lens} being the focal length of the imaging lens. The focal plane (object side) is defined, in the present context, as the plane at which an object forms a focused image on the camera chip. If a particle is at the distance z_{P} from the focal plane, then the image side plane, at which a focused image is formed, moves away from the camera chip. Instead, a new image plane is located at $z_{\text{I2P}}^{\text{defoc}}$, see the second image plane in figure 2. The position of the new image plane $z_{\text{I2P}}^{\text{defoc}}$ can again be calculated from the thin lens equation with z_{P2F} replaced by $z_{\text{P2F}} + z_{\text{P}}$. Note that if the surrounding medium has a refractive index other than $n_2 = 1$, all lengths must be divided by the refractive index of their respective medium. By rearranging equation (4), the distance between the new focal plane and the camera chip can be determined via $(z_{\text{I2P}}^{\text{foc}} - z_{\text{I2P}}^{\text{defoc}})$. With the knowledge of the distance $z_{\text{I2P}}^{\text{foc}}$ from

the calibration $z_{\mathrm{I2P}}^{\mathrm{defoc}}$ can be determined and inserted into the thin lens equation to obtain the distance between the particle and the lens ($z_{\mathrm{P2F}} + z_{\mathrm{P}}$), which in turn can be used to determine z_{P}.

Note that when combining IPI with the defocusing approach, the z-position of the particle z_{P} is related to the PI diameter d_{PI} and the size of the particle d_{P} is related to the frequency F of the PI pattern.

3. The FM—direct problem

To perform IPI with an InvP approach, the first step is to build a FM that is sufficiently accurate to the extent that the model error is significantly less than the measurement error. A spherical particle producing a PI has four parameters of interest described by the vector $\psi_{\mathrm{P}} = (x_{\mathrm{P}}, y_{\mathrm{P}}, z_{\mathrm{P}}, d_{\mathrm{P}})^{\mathrm{T}}$, which are the three-dimensional coordinates of the position and diameter of the particle. The FM should produce a simulated PI based on the particle parameters ψ_{P} and additional hyperparameters $\mathbb{H}$ unrelated to the particle (i.e. wavelength of light λ, focal length of the imaging lens f, parameters describing the optical system M_{tot}, etc). In the following, the FM consists of two cascaded sub-models: A first model for the light scattering at the particle, and a second subsequent model for the wave propagation from the particle to the camera chip through the optical system. To guide the reader through the approach, a schematic flow chart of the algorithmic implementation of the FM is provided in figure 3.

3.1. Scattering model

The scattering process at the particle is influenced by the particle diameter d_{P} and the two hyperparameters θ and m. For a large field of view, the scattering angle can furthermore become a function of the particle position. Assuming that the scattering plane is in the x–z plane, the scattering angle becomes $\theta_{(x_{\mathrm{P}}, z_{\mathrm{P}})} = \theta_0 + \tan(x_{\mathrm{P}}/(z_{\mathrm{P2F}} + z_{\mathrm{P}}))$, which is a function of the particle position with θ_0 being the scattering angle of a particle on the optical axis ($x_{\mathrm{P}} = 0$). For the propagation model, three important details about the GPs must be provided by the scattering model: The position of the GPs in the object plane, the intensity of the light at each GP and the phase difference between the two GPs. The scattering process is best described by the Lorenz-Mie theory (LMT), a solution of the Maxwell equations for a homogeneous sphere [28]. However, as determining the GP position with the LMT is computationally expensive, the GP positions and their phase differences is determined using the GO model. The LMT will then just be used to identify the intensity $I = |S_{\mathrm{GP}}|$ of the light at these GPs, with S_{GP} being the complex amplitude of the light wave emitted from the GP. An equation describing the GO model for a sphere of arbitrary refractive index has been provided by Van de Hulst [29] i.e.

$$\left(\beta_{\mathrm{i}}^{(p)} - p \arccos\left(\frac{1}{m}\cos\left(\beta_{\mathrm{i}}^{(p)}\right)\right)\right) = 2\pi k + q\theta \tag{6}$$

where $\beta_{\mathrm{i}}^{(p)}$ is the angles of the incidence light beam at the particle surface with respect to the surface tangent. The corresponding transmitted angle $\beta_{\mathrm{t}}^{(p)}$ of the refracted ray is already substituted by $\beta_{\mathrm{i}}^{(p)}$ and Snell's law. The constants $k \in [0, 1, 2, \ldots]$ and $q \in \{-1, 1\}$ have to be determined depending on the scattering order and the relative refractive index. The GP position $w^{(p)}$ is then obtained from $w^{(p)} = q\cos\left(\beta_{\mathrm{i}}^{(p)}\right)$. A fast algorithm for this calculation has been proposed by Sax *et al* [23]. This algorithm is used in the present work to compute the positions of the GPs w_j of each order $p = j$ with respect to the centre of the particle projection, see figure 4.

The second quantity to be provided by the scattering model is the phase difference of the wave between the GPs. For the propagation model, the GPs of a particle are assumed to be in the same x–y plane. Therefore, to obtain the phase difference, the different paths of the light rays from the incoming plane to the object plane can be used, taking into account the refractive index of the respective medium. Knowing the angles β_{i} and β_{t}, the travelled distance of the light can be calculated again from optical considerations for $p = 0$ via

$$l_0 = d_{\mathrm{P}} \frac{\sqrt{1 - w_0^2}}{n_2} \tag{7}$$

and the refracted orders $p > 0$ via

$$l_p = d_{\mathrm{P}} \left(\frac{\sqrt{1 - w_p^2}}{n_2} + p \frac{\sqrt{2\,(1 - \cos(2\beta_{\mathrm{t}}))}}{2n_1} \right). \tag{8}$$

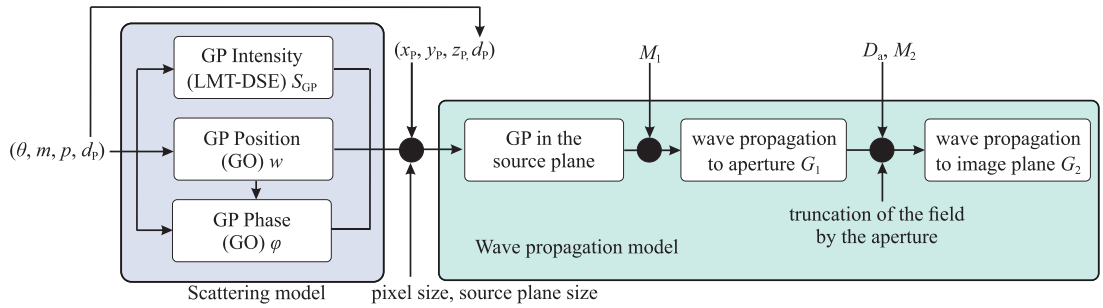

Figure 3. Schematic flow chart of the algorithmic implementation of the FM. To simulate the image of a GP on the camera chip, first the scattering model computes the parameters of the GP in the source plane (intensity, position and phase). This information is then passed to the scattering model to compute the GP image based on the GP as a point emitter in the source plane.

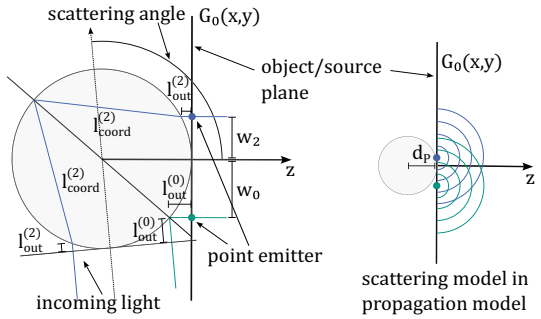

Figure 4. Scattering model (left) and its integration into the propagation model (right) visualized. Incident light is scattered at the particle. The scattering orders $p = 0$ and $p = 2$ and the position of the GPs w_0 and w_2 are shown. The distance travelled from the incident plane to the object plane is in the surrounding medium l_{out} or inside the particle l_{coord}. The GPs are then modelled as point emitters in the source plane. The length l_{out} allows both GPs to be modelled in the same plane.

In addition, the 180° phase shift of a reflection on a medium of higher optical density must be considered. For a reflection on the outside of the sphere, as in the case of $p = 0$, the phase kick-back function $\Delta\varphi_{external}$ is

$$\Delta\varphi_{external} = \begin{cases} \pi, & m > 1 \\ 0, & \text{otherwise.} \end{cases} \tag{9}$$

In case of an internal reflection as for scattering orders $p > 0$ the function is

$$\Delta\varphi_{internal} = \begin{cases} \pi, & m < 1 \\ 0, & \text{otherwise.} \end{cases} \tag{10}$$

The total phase difference is then computed from

$$\Delta\varphi_0 = 2\pi\frac{l_0}{\lambda} + \Delta\varphi_{external} \quad \text{for} p = 0, \tag{11}$$

$$\Delta\varphi_1 = 2\pi\frac{l_1}{\lambda} \quad \text{for} p = 1 \text{ and} \tag{12}$$

$$\Delta\varphi_p = 2\pi\frac{l_p}{\lambda} + (p-1)\,\Delta\varphi_{internal} \quad \text{for} p > 1. \tag{13}$$

This model provides the phase difference between the GPs. However, it should be noted that this GO model neglects the effect of surface waves and the resulting effect on the phase of the GPs. Therefore, the GO-based phase model is a slight oversimplification and the FM will accordingly have some minor deviations from reality. The phase of the wave affects the position of the stripes of the interference pattern in the PI. However, the frequency of the interference pattern, in contrast, is not affected by the

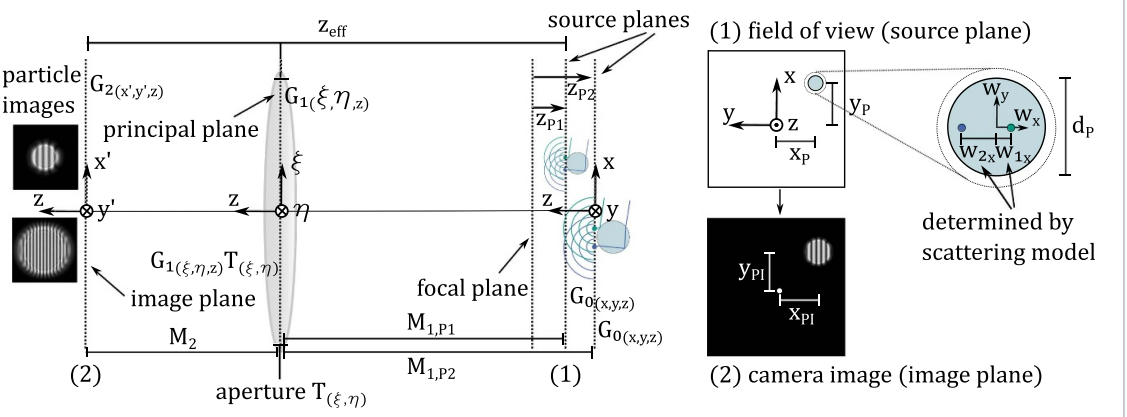

Figure 5. Propagation model and the incorporation of the scattering model visualized. Two particles (double emitters) are shown in a simple optical system consisting of a single lens with an aperture. The GPs of each particle are located in their respective source plane, which has a distance of z_P from the focal plane of the optical system. The field in the source plane is G_0. The lens and aperture are located in the principal plane. The field G_1 in the principal plane is clipped by the aperture function T. The cropped field $G_1 T$ then propagates to the image plane to form the field G_2 which is the final image seen by the camera $G_{\text{image}} = |G_2|$. Also shown are the coordinates of a particle in the source plane (x_P, y_P) and its counterpart (x_{PI}, y_{PI}) of the particle image in the image plane.

phase. Therefore, in the following, only this frequency is considered as the main feature to determine the particle diameter d_P. For a more accurate phase model, the position of the stripes could also be used to fine tune d_P.

Finally, the intensity of each GP depends on the size of the particle, the scattering angle and the refractive index. The GP intensity must be known, because it influences the magnitude of the constructive interference maxima and the destructive interference minima in the PI. The intensity of each GP S_{GP} is calculated from the Debye series expansion (DSE) of the LMT [35, 36]. This can be done efficiently by expressing the derivatives of the Bessel function through recurrence formulae. To compute the GP intensity a custom MATLAB implementation is used for the computation of the Mie coefficients that follows the stable downward recurrence method of Shen *et al* [37] in combination with Lentz's continued fraction method [38], and the Mie angular functions are computed using the functions proposed by Maetzler [39]. The implementation has been validated against MiePlot [40] on bubbles ($m = 1/1.333$) and droplets ($m = 1.333$) in the range of $d_P = [10\,300]$ µm and $\lambda = 532$ nm.

3.2. Wave propagation model

The wave propagation model uses the position (x_{GP}, y_{GP}, z_P), intensity S_{GP} and phase φ of each GP to model the propagation of light waves through the optical system to the camera chip. Since interference and diffraction must be taken into account, a wave model is used. The model chosen for wave propagation is the Huygens–Fresnel integral, which is an approximation of the Rayleigh-Sommerfeld diffraction theory assuming that the source (object) plane and image plane are much further apart than their respective sizes. The Huygens–Fresnel integral calculates the field $G_2(x', y', z)$ in a plane (x', y') (here the camera chip) at a distance z from the source plane (i.e. the position of the particle) based on the field $G_0(x, y, z = 0)$ in the source plane at $z = 0$, see G_2 and G_0 in figure 5. The propagation model calculates the waves based on the position of the source plane z_P, i.e. the positions of the GPs. Therefore, the particle diameter is added to z_P to obtain the true position of the particles centre $(z_P + d_P/2)$, compare the right side of figure 4. While the Huygens–Fresnel integral only describes the propagation of spherical waves in free space, the introduction of a RTM allows the integral to be generalized to arbitrary optical systems [41]. For optical systems that differ in the x–z plane and the y–z plane, the generalized Huygens–Fresnel integral can be written as [41, 42].

$$G_2(x', y', z = z_{\text{eff}}) = -\mathrm{i}\frac{k}{2\pi\sqrt{B^x_{\text{tot}} B^y_{\text{tot}}}} \exp(\mathrm{i}kz_{\text{eff}}) \iint G_0(x, y, z = 0) \exp\left(-\frac{\mathrm{i}k}{2B^x_{\text{tot}}}\left[D^x_{\text{tot}} x^2 - 2x'x + A^x_{\text{tot}} x'^2\right]\right) \times \exp\left(-\frac{\mathrm{i}k}{2B^y_{\text{tot}}}\left[D^y_{\text{tot}} y^2 - 2y'y + A^y_{\text{tot}} y'^2\right]\right) \mathrm{d}x\mathrm{d}y, \tag{14}$$

where $z_{\text{eff}} = \sum_\ell z_\ell / n_\ell$ is the effective distance from the source plane to the image plane, and z_ℓ are the individual distances travelled in the media of refractive index n_i. The in-plane coordinates are (x, y) in

the source plane (referring to x_P and y_P) and (x',y') in the image plane (referring to x_PI and y_PI). The components $A^x_\mathrm{tot}, B^x_\mathrm{tot}, D^x_\mathrm{tot}$ describe the optical system in the x–z plane and the components $A^y_\mathrm{tot}, B^y_\mathrm{tot}, D^y_\mathrm{tot}$ describe the optical system in the y–z-plane. Equation (14) allows the field G_2 to be obtained even when optical elements such as lenses and glass walls are placed between the source and the image plane. For most optical systems, however, a limiting aperture must be taken into account. A solution to this problem was presented by Wen *et al* [43, 44], where the problem is solved in two steps: Propagation from the source plane to the principal plane (location of the aperture) and propagation from the principal plane to the image plane, see the notations G_0, G_1, G_1T, G_2 in figure 5. Starting with the field in the source plane $G_{0(x,y,z=0)}$, the field at the aperture $G_1(\xi,\eta,z=z_\mathrm{aperture})$ is calculated according to equation (14). The field G_1 is then cropped by the aperture, which is modelled by multiplying G_1 with a transmission function $T(\xi,\eta)$ in the aperture plane. This transmission function is close to one within the aperture radius and zero elsewhere. A model for such an aperture function as a superposition of Gaussian functions was proposed by Wen *et al* [43, 44] as

$$T(\xi,\eta)=\sum_{\ell=1}^{N}P_\ell\exp\left(-\frac{Q_\ell}{(D_\mathrm{a}/2)^2}\left(\xi^2+\eta^2\right)\right) \tag{15}$$

with the complex coefficients P_ℓ and Q_ℓ which can be found in [43, 44] and the aperture diameter D_a. The field at the image plane $G_{2(x',y',z=z_\mathrm{eff})}$ is then calculated again with equation (14) based on the cropped field $G_{1(\xi,\eta,z=z_\mathrm{aperture})}T_{(\xi,\eta)}$. For this, the RTM $M^{(x,y)}_\mathrm{tot}$ is split into two subsystems describing the optical system from the source plane to the principal plane $M^{(x,y)}_1$ and from the principal plane to the image plane $M^{(x,y)}_2$.

The majority of the light on the particle surface (seen from the scattering angle θ) is caused by the GPs. Following Shen *et al* [27] a GP can be approximated as a point source of light at a known position, intensity and phase (i.e. the output of the scattering model). The source field for a single GP is then $G_{0(x,y,z=0)}=S_\mathrm{GP}\delta_{(x-x_\mathrm{GP},y-y_\mathrm{GP})}$ with the complex amplitude of the emitted wave S_GP, which includes the intensity and phase of the GP, and the Dirac function δ. The peak of the Dirac function is placed at the coordinates

$$\begin{pmatrix}x_\mathrm{GP}\\ y_\mathrm{GP}\end{pmatrix}=\begin{pmatrix}x_\mathrm{P}+w_x d_\mathrm{P}\\ y_\mathrm{P}+w_y d_\mathrm{P}\end{pmatrix} \tag{16}$$

based on the relative position of the GP on the particle surface $w_{x,y}$ provided by the scattering model, see the particle close up in figure 5. For most IPI applications, a scattering plane in either the x–z or x–y plane is chosen so that the $w_{x,y}$ component outside the plane is zero. The Dirac function greatly simplifies the solution of the integral, and an analytical solution for G_2 can be given directly from the source field G_0 for a single GP [27]:

$$G_2(x',y',z_\mathrm{eff})=\frac{\exp\left(\mathrm{i}\frac{2\pi}{\lambda}z_\mathrm{eff}\right)\exp\left(\mathrm{i}\frac{\pi}{\lambda}\left(\frac{D^x_2x'^2}{B^x_2}+\frac{D^y_2y'^2}{B^y_2}\right)\right)}{(\mathrm{i}\lambda)^2\sqrt{B^x_1B^y_1B^x_2B^y_2}}\sum_\ell^{N_\ell}\frac{P_\ell\pi}{\sqrt{\gamma_{x,(\ell)}\gamma_{y,(\ell)}}}S_\mathrm{GP}\exp\left(\beta_{(\ell)}+\mathrm{i}\varphi\right) \tag{17}$$

with the following abbreviations

$$\beta_\ell:=\mathrm{i}\frac{\pi}{\lambda}\frac{A^x_1}{B^x_1}x^2_\mathrm{GP}+\mathrm{i}\frac{\pi}{\lambda}\frac{A^y_1}{B^y_1}y^2_\mathrm{GP}-\frac{\phi^2_{x'}}{4\gamma_{x,(\ell)}}-\frac{\phi^2_{y'}}{4\gamma_{y,(\ell)}} \tag{18}$$

$$\gamma_{x,\ell}:=\frac{4Q_\ell}{D^2_\mathrm{a}}-\mathrm{i}\frac{\pi}{\lambda}\left(\frac{D^x_1}{B^x_1}+\frac{A^x_2}{B^x_2}\right) \tag{19}$$

$$\gamma_{y,\ell}:=\frac{4Q_\ell}{D^2_\mathrm{a}}-\mathrm{i}\frac{\pi}{\lambda}\left(\frac{D^y_1}{B^y_1}+\frac{A^y_2}{B^y_2}\right) \tag{20}$$

$$\phi_{x'}:=\frac{2\pi}{\lambda}\left(\frac{x_\mathrm{GP}}{B^x_1}+\frac{x'}{B^x_2}\right) \tag{21}$$

$$\phi_{y'}:=\frac{2\pi}{\lambda}\left(\frac{y_\mathrm{GP}}{B^y_1}+\frac{y'}{B^y_2}\right). \tag{22}$$

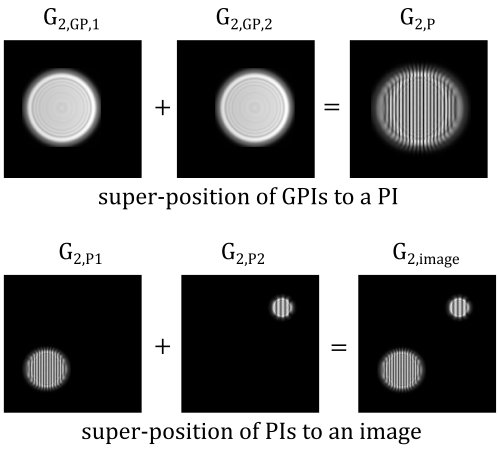

Figure 6. The superposition principle for the construction of a PI from the individual GPIs is visualized (top). The construction of a full camera image with multiple PIs is shown in the lower half (bottom).

Equation (17) gives the field in the image plane for a single GP. Particles such as opaque tracer particles in DPTV can be modelled as single emitters and equation (17) adequately models such a single emitter particle. For particles such as bubbles and droplets in IPI, the particle is modelled as a double (or triple) emitter from its GPs $(x_{j,\mathrm{GP}}, y_{j,\mathrm{GP}})$ with $j = 1, 2, \ldots, N_{\mathrm{GP}}$, where N_{GP} is the number of GPs of a particle (usually $N_{\mathrm{GP}} = 2$). The final field of a particle image $G_{2,\mathrm{P}}$ is then modelled as a superposition of the complex fields (GPIs) produced by its individual GPs $G_{2,\mathrm{GP},j}$

$$G_{2,P}(x', y', z = z_{\mathrm{eff}}) = \sum_{j=1}^{N_{\mathrm{GP}}} G_{2,\mathrm{GP},j}(x', y' z = z_{\mathrm{eff}}) \; ; \tag{23}$$

see the upper part of figure 6. To obtain the full image $G_{2,\mathrm{image}}$ of multiple particles, the complex fields $G_{2,\mathrm{P},\ell}$ of individual particles ℓ are superimposed and the absolute value of the result gives

$$G_{\mathrm{image}}(x', y') = \left| \sum_{\ell=1}^{N_{\mathrm{P}}} G_{2,P,\ell}(x', y', z = z_{\ell,\mathrm{eff}}) \right| \tag{24}$$

with N_{P} number of particles, compare the lower part of figure 6.

If IPI is to be performed in a volume, each particle ℓ might be located at a different z-position. Therefore, does this model contain a separate source plane for each particle ℓ, but only one common image plane (i.e. the location of the camera chip). Accordingly, also the RTM $M_{1,\ell}$ (i.e. source plane to principal plane) might be different for each particle ℓ as it is a function of the z-position of the particle $z_{\mathrm{P},\ell}$. The RTM M_2 (describing the propagation from the principal plane to the image plane) is the same for all particles.

3.3. Validation of the FM

The sub-models used for the scattering model have already been validated in the literature [27, 29] and the GO model is commonly used to model the scattering process in IPI [1, 18]. Therefore, only the full FM needs to be validated for the accuracy of the PI diameter as a function of the particle's z-position and for the correct representation of the PI's interference pattern for a given particle size.

To validate the PI diameter d_{PI} of the model, a simple single lens system is modelled, similar to the one shown in figure 2. The system consists of a single lens of focal length $f_{\mathrm{lens}} = 105\,\mathrm{mm}$ and finite aperture (aperture number 4 corresponding to the aperture diameter $D_{\mathrm{a}} = f_{\mathrm{lens}}/4$) and an image plane located at $z_{\mathrm{I2F}} = 200\,\mathrm{mm}$. The corresponding focal plane is at $z_{\mathrm{P2F}} = 221.1\,\mathrm{mm}$. The values for $f_{\mathrm{lens}}, D_{\mathrm{a}}$ where chosen from the validation experiment in order to have realistic parameters. A single emitter particle is simulated at different distances from the focal plane. The resulting grey value intensities across the PI are plotted in figure 7. The FM shows a good agreement of the PI diameter with the Olsen-Adrian model [34] and with the GO model [27]. It can also be seen in figure 7 that the loss of intensity with increasing defocus is captured by the model. This means that the intensity of the PI can be used as an additional feature for the IP.

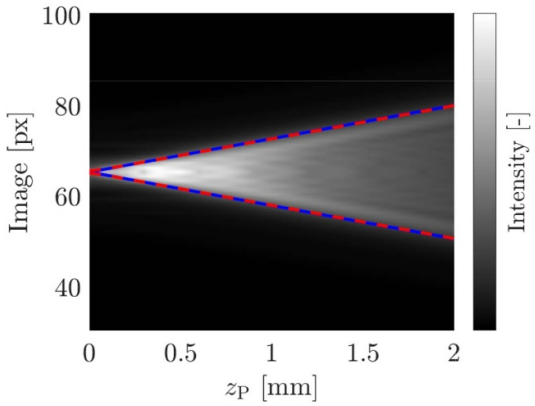

Figure 7. Grey value intensity distribution of the imaged PI field for different distances z_P from the focal plane as computed with the forward model. For comparison, the theoretical PI diameter according to the Olsen-Adrian model [34] (•) and the GO model from equation (4) (•) are converted to pixels and added to the diagram.

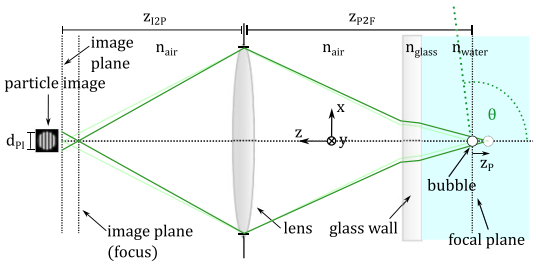

Figure 8. Optical system of the experiment used to obtain the experimental PIs of the bubbles. The bubbles are located at a distance z_P from the focal plane. The focal plane is located in a water tank behind a glass wall. The imaging system is a single lens with an aperture in the principal plane. The camera chip is located in the image plane. The refractive indices of each part of the optical system are given.

Equation (17) has been validated to accurately represent the interference pattern for droplets [27]. Therefore, the FM is validated here on an experiment with bubbles ($m = 1/1.333$). The images used to validate the model are images from the experiment described by [23].

The optical setup is shown in figure 8. The bubbles are located at a distance z_P from the focal plane, in a water tank with $n_2 = n_{water} = 1.333$. The focal plane is located in the water with a distance of $z_{water} = 208.3$ mm from the glass wall (thickness $z_{glass} = 4$ mm). The glass wall is located at a distance of $z_{air} = 117.1$ mm from the principal plane. At the principal plane an imaging lens with a limiting aperture is located (Nikon Micro-Nikkor $f_{lens} = 105$ mm, $D_a = f_{lens}/4$). Finally the image plane (camera chip) has a distance of $z_{image} = 211.8$ mm from the principal plane. The camera used in the experiment was a PCO Pixelfly (pixel size 6.45 µm) and the bubbles were illuminated with a Quantel Evergreen Nd:YAG laser ($\lambda = 532$ nm) at a scattering angle of $\theta = 99°$. The scattering angle of 99°, was chosen as the measurement uncertainty is the lowest at this scattering angle for the given particle sizes [23]. Further information on the experiment can be found in [23].

The imaging lens is modelled as a thin lens in the principal plane. The effective optical path length of the system is $z_{eff} = (z_{image} + z_a)/n_a + z_g/n_g + (z_w + z_P)/n_w$, where z are distances and n refractive indices. The corresponding RTM from lens to camera chip is

$$M_2^{x,y} = \begin{bmatrix} 1 & z_{image} \\ 0 & 1 \end{bmatrix} \tag{25}$$

and the RTM from particle to lens is

$$M_1^{x,y} = M_{lens} M_{p,a} M_{I,g\to a} M_{p,g} M_{I,w\to g} M_{p,w} M_{p,P(z_P)}, \tag{26}$$

where $M_{p,j}$ represents propagation through free space, $M_{I,n_1\to n_2}$ represents a flat interface from medium n_1 to medium n_2 and M_{lens} describes a thin lens. The indices a, w, g represent air, water and glass respectively.

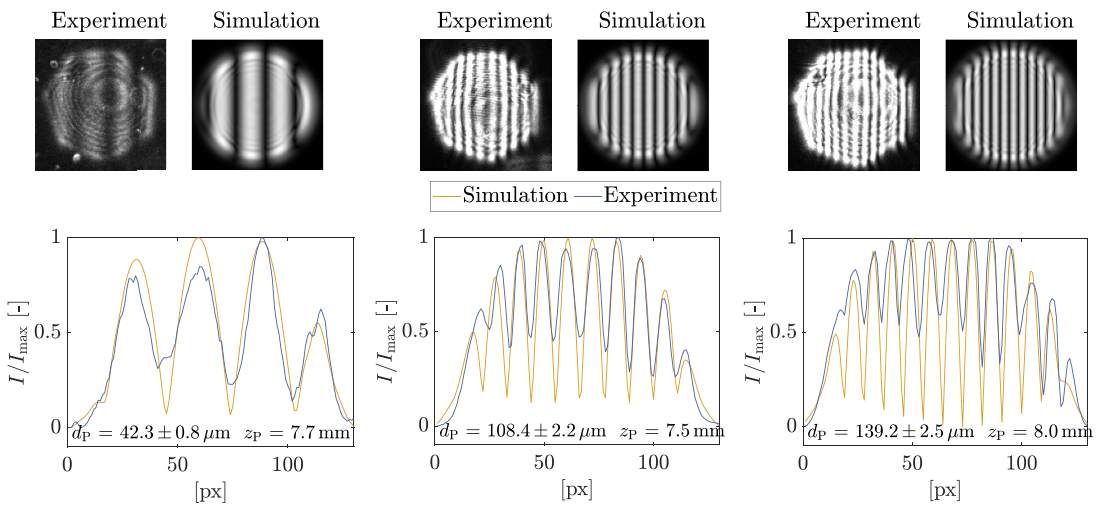

Figure 9. Experimental (left) and simulated (right) particle images for three different bubble sizes (top). In the bottom row the signal from averaging the PI along the stripes of the pattern is shown. Below each graph the used z-position and size of each bubble is displayed. The uncertainty of the size estimation with the FFT approach is also displayed. The size of the particle was only varied within a tenth of the uncertainty of the FFT approach to obtain the simulated image.

In the validation experiment, the z-position of the bubbles was measured by fitting the PI diameter with a circular Hough transform. The determination of the PI diameter by this method is at least pixel accurate [15]. For the given optical system an error of $\Delta d_{PI} = 1\,px$ results in an uncertainty of $\Delta z_P = 81.4\,\mu m$ according to equations equations (4) and (5). A widely spread method to interpret the interference pattern in IPI is the extraction of the fringe frequency by applying a Fourier transformation to the fringe pattern and fitting the frequency peak in frequency space [30, 45, 46]. This method is, therefore, used as the benchmark in the present work. To determine the size of the bubble, the PI was averaged along the stripes of the interference pattern and the resulting signal, as plotted in figure 9, was processed by an FFT. The signal was zero-padded by a factor of 10. Analogous to [23], the PI was split up into four different segments perpendicular to the stripes (upper-kernel, middle-kernel, lower-kernel and full-kernel). The four image kernels where then processed individually to obtain the experimental variance of the FFT processing. The particle size was determined using equation (1). To obtain the diameter uncertainty of the method, the kernel with the largest frequency was paired with $z_P + \Delta z_P$ and the kernel with the smallest frequency was paired with $z_P - \Delta z_P$. This gives the maximum spread of possible diameters. The determined z-position and diameter were then used in the FM to simulate the PIs, which are shown in figure 9. Since the FFT approach has an estimation uncertainty, the bubble diameter for the FM was varied, starting from the mean diameter of the FFT approach, to best fit the experimental PI. The bubble size was varied only within a tenth of the uncertainty interval of the FFT approach. It can be seen that for different bubble sizes a great agreement between the simulated PIs and the real experimental PIs was achieved within the measurement uncertainty of the FFT approach. In the experiment a heptagonal aperture was used which the model fails to capture as the aperture function T assumes a circular aperture. However, the match of PI diameter and the intensity distribution of the fringes match closely as can be seen in figure 9. Due to the heptagonal shape of the aperture, the outer most stripes of the averaged signal differ slightly. This is, however, an artefact of averaging along the stripes, where the shape of the aperture affects the height of the averaged maxima. Another discrepancy between the FM and the experiment is the location of the Newton-rings (i.e. diffraction at the aperture) within the PI. As the FM model uses the paraxial approximation, the Newton-rings are always centred in the PIs, unlike in reality where the centre of the Newton-rings depends on the in-plane position of the PI. Over all, the FM represents reality sufficiently and can be used for the InvP approach.

4. IP for a single particle

In this section the InvP for a single double-emitter particle is considered. The simulation of multiple particles follows in section 5. A single double emitter (bubble or droplet) is characterized by the parameter vector $\psi_P = (x_P, y_P, z_P, d_P)^T$. To optimize this vector, an interior-point algorithm [47] with numerical gradients by means of central differences is applied. This work uses MATLAB's implementation of

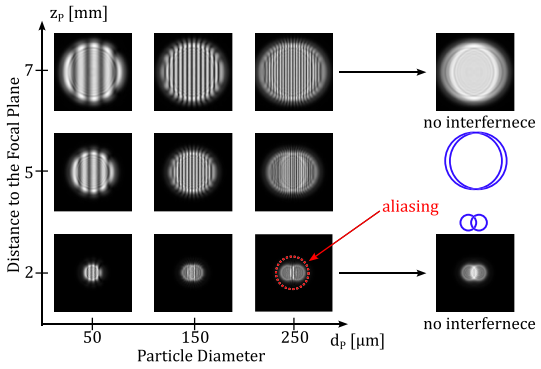

Figure 10. Particle images for different particle diameters and distances from the focal plane. Larger particles require greater distances from the focal plane to be sufficiently defocused (i.e. the PI resembles a single circle). PIs without interference, as created with equation (27), are shown, to visualize the double circle nature of double emitter PIs (cp. also the blue circles). The images without interference are used to calculate $\mathcal{P}_{\mathrm{P,pos}}$. The influence of the particle diameter in combination with the z-position on the PI shape becomes obvious, when omitting the interference. Also the effect of aliasing as a function of diameter and z-position can be observed as marked by the red circle. Recall that aliasing can occur in two ways, where either the particle becomes larger with accordingly increasing number of fringes or the PI becomes smaller, such that the remaining PI-intersection for the fringes diminishes.

the *fmincon*, which uses a trust-region interior point algorithm [48], to minimize a mismatch functional $\mathcal{P}_{(\psi_\mathrm{P})}$ that assesses the similarity between the simulated and the real (observed) image G_{obs}. Note that the same methodology can also be applied to a DPTV only approach locating tracer particles. In this case, a particle is modelled as a single emitter and the optimization vector is shortened to $\psi_\mathrm{P}^{\mathrm{Tracer}} = (x_\mathrm{P}, y_\mathrm{P}, z_\mathrm{P})^\mathrm{T}$.

4.1. Mismatch functionals for the optimization

the InvP approach requires suitable mismatch functionals for the optimization. For the position of the particle $(x_\mathrm{P}, y_\mathrm{P}, z_\mathrm{P})^\mathrm{T}$ the *Structure Similarity Index* SSIM [49] was identified to be a robust choice. The particle is modelled as a double emitter, which leads to the optimization vector $\psi_{\mathrm{P,pos}} = (x_\mathrm{P}, y_\mathrm{P}, z_\mathrm{P}, d_\mathrm{P})^\mathrm{T}$. An IPI particle is modelled as a double emitter due to the double-circular nature of the PIs and the influence of the particles diameter on the PI shape, see figure 10. While the global minimum of the SSIM mismatch functional is in the correct position, it appears to be non-smooth and has many local minima. This is due to the stripes of the interference pattern in the PI. To mitigate this problem, the particle image is simulated without stripes. In order to avoid the stripes due to interference, the two glare point images (GPI) $G_{2,\mathrm{GPj}}$ are not superimposed until after the absolute value of the field has been taken, i.e.

$$G_{\mathrm{P,pos}} = |G_{2,\mathrm{GP1}}| + |G_{2,\mathrm{GP2}}|. \tag{27}$$

In this way, the complex amplitude is omitted and no interference appears. The resulting PI obtains only the shape of the PI but not the interference pattern, as indicated in figure 10. The mismatch functional for the particle position therefore goes as

$$\mathcal{P}_{\mathrm{P,pos}}\left(\psi_{\mathrm{P,pos}}\right) = -\mathrm{SSIM}\left(G_{\mathrm{P,pos}}\left(\psi_{\mathrm{P,pos}}\right), G_{\mathrm{obs}}\right) \tag{28}$$

with a negative sign as the SSIM approaches a positive maximum ($\mathcal{P}_{\mathrm{P,pos}} = 1$) for a perfect match.

To formulate a mismatch functional for the diameter $\mathcal{P}_{\mathrm{P,dia}}$, the fringe frequency should be considered as the main feature. Simply comparing both G_{image} with the observed (i.e. recorded) image G_{obs} for different particle diameters d_P leads to the same problem of a non-smooth objective functional with many local minima, due to the stripes in the PI. Varying the particle diameter changes the fringe frequency, and whenever stripes of the simulated and observed images overlap, there is a local minimum, even if the fringe frequency of the pattern is not the same. In addition, the phase difference between the GPs causes the stripes to move perpendicular to the stripe orientation as the particle diameter increases, creating even more local minima between the fringe frequency multiples. Both of these effects render a simple comparison of the simulated image with the observed image infeasible for a local search and would require an expensive global search. Therefore, the Fourier-transformed images are compared instead. This eliminates the phase-induced shift of the stripes and multiples of the fringe frequency are clearly distinguishable. Since noise in the observed image introduces additional frequencies, the normalized cross-correlation of the two Fourier transformed images is chosen as the mismatch functional. The

mismatch functional for the diameter is

$$\mathcal{P}_{\mathrm{P,dia}} = -\left(\mathcal{F}_2\left\{G_{\mathrm{image}}\right\} \star \mathcal{F}_2\left\{G_{\mathrm{obs}}\right\}\right), \tag{29}$$

where $\mathcal{F}_2$ denotes a two-dimensional FFT and the $\star$ symbol denotes a normalized cross-correlation. For better accuracy, the simulated and observed images can be zero-padded similar to the FFT approach. However, this increases the size of the processed image in pixel space, so a factor of two zero padding was used in this work to limit the computational cost. This mismatch functional has a global minimum for a matching diameter, but is only monotone and smooth near the global minimum. Other local minima exist further away from the minimum, making the diameter determination the most challenging part.

Since both mismatch functionals are in the same range, $\mathcal{P}_{\mathrm{P,pos}} \in [-1,0]$ and $\mathcal{P}_{\mathrm{P,dia}} \in [-1,0]$ they can be combined to formulate the combined mismatch function $\mathcal{P}_{\mathrm{P}} = \mathcal{P}_{\mathrm{P,pos}} + \mathcal{P}_{\mathrm{P,dia}}$. In this way, the characteristic of the PI shape changing with particle size can be taken into account in addition to the fringe frequency.

4.2. Optimization strategy for a single particle

Optimizing over all four particle parameters by means of a local search likely means a termination in a local minimum rather than the global one, due to the non-convex nature of the optimization function. However, for a reliable parameter estimation, a minimum as close as possible to the global minimum must be found. As discussed in the last section, the mismatch function for particle size is only quasi-smooth near the global minimum. Therefore, initialization close to the global minimum is required to ensure reliable convergence of the algorithm. Recent advances in PI detection [12–15] for DPTV approaches allow for at least pixel accurate placement of bounding boxes (BB) around the PI. The placement of a BB provides values on the PI $(x_{\mathrm{PI}}, y_{\mathrm{PI}}, d_{\mathrm{PI}})$. Initial values for the in-plane position of the particle $(x_{\mathrm{P}}, y_{\mathrm{P}})$ can be derived directly from the PI position $(x_{\mathrm{PI}}, y_{\mathrm{PI}})$ considering the magnification of the system, similar to conventional PTV approaches. An initial guess for the z-position of the particle can be derived from the PI diameter d_{PI}, e.g. via equations equations (4) and (5).

The BB values can then be used to initialize the optimization close to the global minimum. The local search is then constrained to an interval based on the uncertainty of the detection method used. In this work, two BB accuracies are considered: ± 1 px and a more conservative version of ± 5 px. The optimization is constrained to the BB uncertainty to ensure an actual refinement of the initial detection. However, a BB around the PI does not provide information about the particle diameter. Therefore, to obtain an initial estimate of the particle diameter, a global search is performed over the specified diameter interval with a resolution of 50 steps, while keeping the position parameters fixed. In this work the interval of possible diameters $d_{\mathrm{P}} = [20, 300]$ µm is used, where the lower end corresponds to the lower limit of particle diameters measurable with for the given setup (i.e. the minimum diameter for which a full wavelength of the stripe pattern is still in the PI [23]). A global search over the expected range of diameters provides a starting value for the diameter.

As the optimization in high dimensions is difficult, the problem is separated into two sub-problems to reduce the dimensionality of the search: first, only the position $(x_{\mathrm{P}}, y_{\mathrm{P}}, z_{\mathrm{P}})$ is optimized with d_{P} as a free parameter, so that the shape of the simulated PI is closer to the observed PI, compare the double circle nature of the PI shown in figure 10. In this step, only $\mathcal{P}_{\mathrm{P,pos}}$ is used, so that changes in d_{P} only affect the double circular shape of the PI and stripes are omitted. This bears the advantage of smoothing the mismatch functional, consequently increasing the chances to find a better local minimum.

In the second step, the particle diameter based on the global search is used to initialize d_{P} as well, using $\mathcal{P}_{\mathrm{P,dia}}$. The optimization then runs over $(z_{\mathrm{P}}, d_{\mathrm{P}})$ with $\mathcal{P}_{\mathrm{P,pos}} + \mathcal{P}_{\mathrm{P,dia}}$ to refine the z-position and diameter by changing the size, shape and interference pattern of the PI. The in-plane position is kept fixed as it only affects the position of the PI, not the shape and pattern. The particle parameters $(z_{\mathrm{P}}, d_{\mathrm{P}})$ are optimized together as the double circular shape and interference pattern of the PI depend on both the z-position (size of the circular GPIs and fringe spacing) and on the diameter (distance of the circular GPIs and the fringe spacing). The combined optimization further reduces the dependence of the diameter determination on the out-of-plane determination, as the two effects that z_{P} and d_{P} have on the PIs are not easily separable. While in standard IPI approach, an error in the z-position directly propagates into the diameter estimation without the chance of correction, the combined optimization allows to correct z_{P} errors while estimating d_{P}, thus avoiding this issue.

An overview over the full method—from the recording of the raw images to the reconstructed particle field—is shown in figure 11. First, images are recorded and processed, e.g. by a CNN to obtain BBs of the PIs, compare the work of [13–15]. The BBs are then used to initialize the parameter vector.

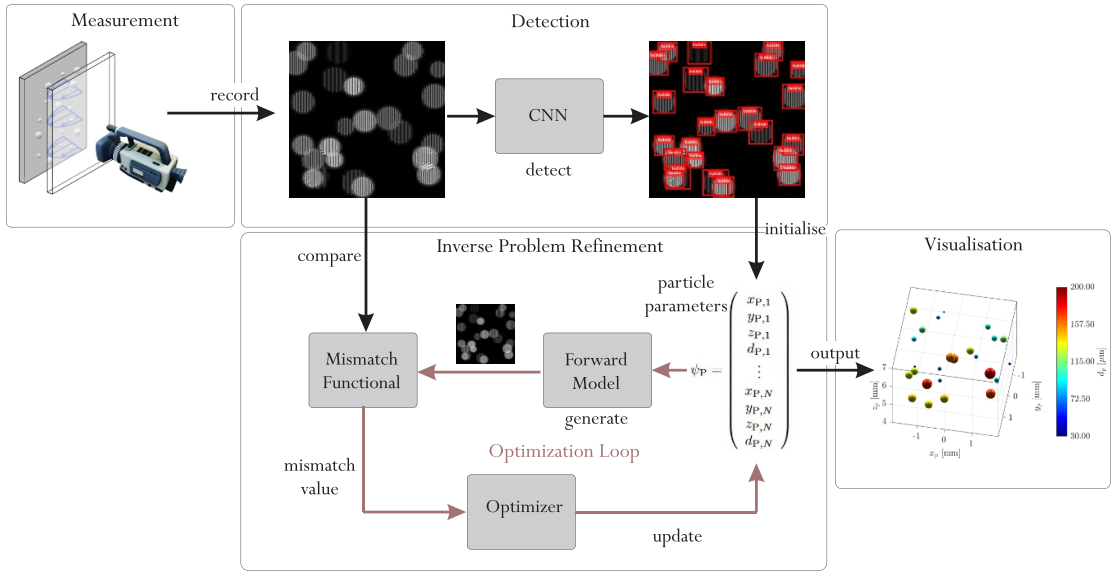

Figure 11. Scheme of the InvP approach in the context of a measurement. First images are recorded and a detection algorithm (e.g. a CNN) is used to generate BBs. The BBs are used to initialize ψ_P and the IP. In the InvP ψ_P is fed into the FM to produce a simulated image. The simulated image is then compared to the observed image by the mismatch functional, which quantifies the mismatch by a single value. This value is then minimized (e.g. by a trust-region interior-point algorithm) until a convergence criterion is reached. The particle field is then reconstructed from the final iteration of ψ_P. the InvP is analogue for a single or for multiple particles.

The parameter vector ψ_P is then fed into the FM and the resulting image into the mismatch functional. The parameter vector is then optimized to minimize the mismatch functional, e.g. with a trust-region interior-point [48] algorithm. Once the optimization terminates, ψ_P can be used to obtain the particle field. The process works analogue for single or multiple particles.

4.3. Test on a single synthetic particle image

To test the InvP approach first synthetic PIs, as generated by the FM, are considered (added Gaussian noise—mean 0.1 and variance 0.1), as the ground truth particle parameters $\hat{\psi}_\mathrm{P}$ are known without uncertainty for synthetic PIs. This also allows for particle parameters to be deliberately modified. For all synthetic tests, the optical system to mimic the bubble sizing experiment is used for the FM.

First, only one particle parameter is optimized, while the other three are kept fix (at ground truth) to investigate the potential limit of the InvP approach. To investigate the diameter accuracy, the diameter is initiated with the global search and then fitted with the local search. An FFT algorithm, as used to size the particles in figure 9 is also applied on the images to act as a bench mark (also with ground truth z-position). Since the InvP approach uses the same FM as used for the generation of the (synthetic) observed image, the InvP approach has a natural advantage over the FFT approach on synthetic images, that will not appear on images from real experiments. However, the effect of different PIs on the InvP and FFT approaches can be assessed independent from this effect. The results are shown in figure 12(a).

Since the particle diameter and its z-position are connected, two cases are tested: First, the particle diameter is kept constant ($d_\mathrm{P} = 100\,\mu\mathrm{m}$) and the PIs are generated at different z-positions. This way the effect of insufficient defocusing can be investigated (i.e. when the GPIs are not sufficiently overlapping, see figure 10 thus leading to the aforementioned aliasing effect). The aliasing effect in the interference pattern appears when the distance between the stripes becomes to small to be resolved by the pixel size (i.e. the Nyquist frequency is reached). As indicated in figure 10, aliasing can occur through two different ways: (i) the particle becomes too large and too many fringes are squeezed into the PI or (ii) the distance to the focal plane decreases and the PI shrinks to that the same amount of fringes becomes squeezed together in a smaller area.

Both the FFT and the InvP approach achieve sub-micrometre accuracy. It can be seen that the InvP approach determines the diameter at least to the same level of accuracy as the FFT approach. The main difference between the FFT and the InvP approach, is that the InvP approach fits the whole spectrum of frequencies in Fourier space, whereas the FFT approach only fits one dominant peak. This renders the InvP approach potentially more robust to overlaps and other imperfections of the PI. While the

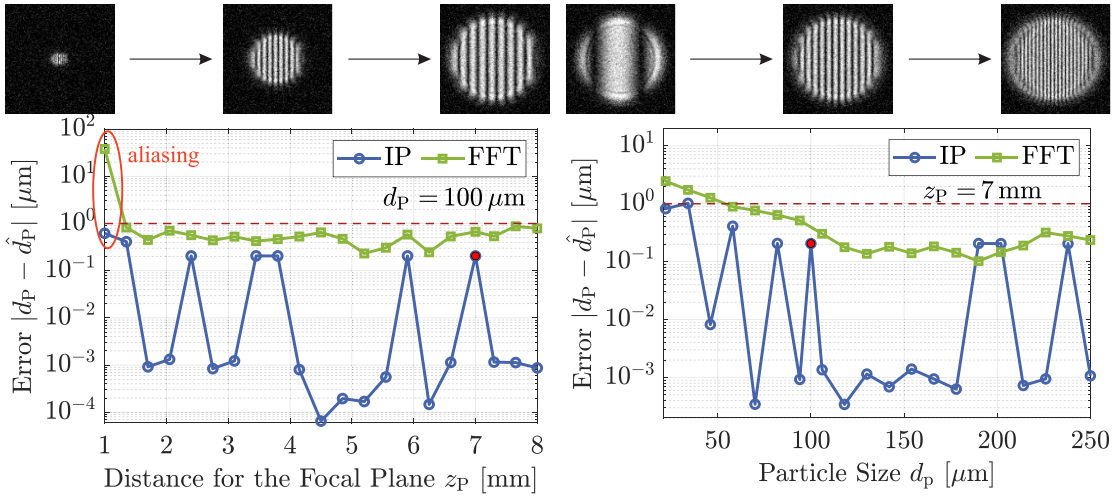

(a) varying z-position (b) varying diameter

Figure 12. IP approach and FFT for the diameter measurement with known particle position (x_P, y_P, z_P). Both approaches were given the ground truth particle position and only the particle diameter was determined. For the simulated observed image, in (a) the particle z-position was varied with a fixed diameter, and in (b) the particle diameter at fixed z-position was varied. The red dashed line (- - -) represents the micro-meter accuracy for the present optical system. The red dot (•) shows where the two test series intersect in parameter space.

optimization on synthetic images reaches errors as low as sub-nanometer levels, this degree of accuracy is unrealistic as the FM is unlikely to represent reality to this degree. Errors smaller than a tenth of a micrometre can be accredited to the InvP approach using the same FM model as the observed images.

A major advantage of the InvP approach over the FFT becoming visible in figure 12(a) (red marking), which is the robustness against aliasing in the interference pattern. It can be seen that the FFT approach fails to function properly when the particle is to close to the focal plane and aliasing occurs, as seen by the sudden increase of error for small z-positions. This sharp increase does not occur for the InvP approach, since the FM can correctly account for the aliasing (due to the known pixel size in the FM and the according discretization of the field G_2). As the FM accounts for aliasing, the InvP can deal with this effect accordingly. This has an important implication: Since aliasing occurs for insufficiently defocused particles (i.e. particles to close to the focal plane for their size), this allows the InvP approach for the measurement of particles closer to the focal plane.

Next, the effect of the particle size on the diameter estimation was tested, see figure 12(b). In this test series the z-position of the particle was kept constant and the diameter was varied. The z-position $z_P = 7$ mm was chosen to ensure sufficient defocusing for all particle diameters. It can be seen that the FFT approach performs better for larger particles (i.e. more fringes in the PI), while the particle size seems to have no visible effect on the InvP approach.

The same two tests (with the same PIs) were conducted with the in-plane position (x_P, y_P) and the diameter d_P kept fixed at known ground truth values and only the z-position was optimized. For this test a BB placement uncertainty of $x_{PI}, y_{PI}, z_{PI} = \pm 1$ px was assumed. Most machine learning methods used for particle detection in DPTV achieve pixel accurate results [13–16]. However, the higher uncertainty was chosen for conservative testing and to account for any placement errors of detection algorithms. The results are shown in figure 13. Overall, it can be seen that the InvP approach achieves sub-pixel accuracy for the z-position in the case of good initialization. The diameter of the particle, and therefore, the shape of the PI, compare figure 10, does not seem to have an observable influence on the z-position uncertainty.

Next the InvP approach is considered for a search over the full optimization vector ψ_P, without any ground truth information. The position initialized from the BB placement with a ± 1 px and a ± 5 px error in a random direction to simulate the BB placement uncertainty of a detection approach. For this test, 200 PIs were generated with random particle parameters ψ_P in $x_P, y_P \in [-1, 1]$ mm, $z_P \in [1, 8]$ mm and $d_P \in [20, 300]$ µm. The distribution of the resulting estimation errors are shown in figure 14 and the median errors are shown in table 1. The in-plane accuracy of the InvP approach is sub-pixel accurate and poses a clear improvement from the pixel accurate BB placement. For single PIs the accuracy of the x and y positions differs, which is a result of the directionality of the fringes in the PI. The directionality causes the objective functional to have a different topology in the x and y dimensions. This

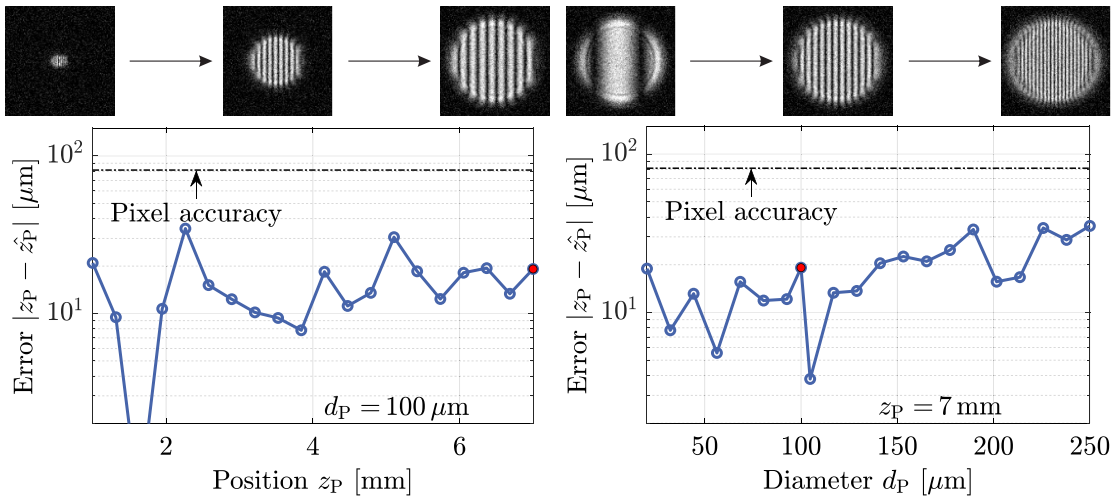

(a) varying z-position (b) varying diameter

Figure 13. Optimization of the particle z-position with the ground truth of the other particle parameters (x_P, y_P, d_P) for a varying z-position and fixed diameter (a) and for a varying diameter with fixed z-position (b). The black dashed line (- - -) represents the pixel accuracy. The red dot (●) shows where the two test series intersect in parameter space.

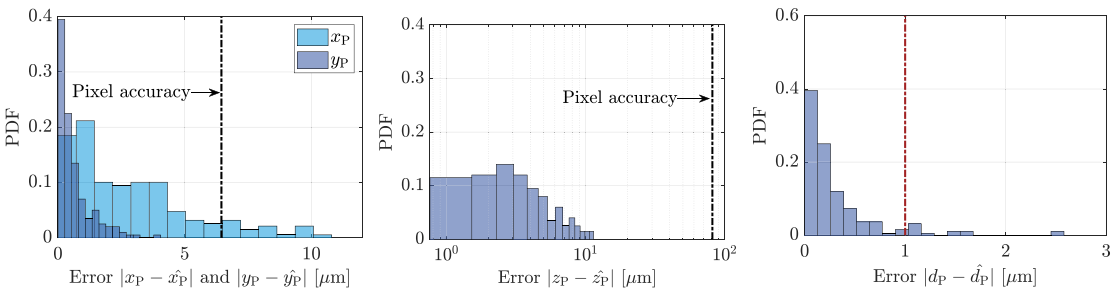

(a) In-plane error (b) Out-of-plane error (c) Diameter error

Figure 14. Probability density function (PDF) of the errors of the InvP approach (1 px initialization error) for 200 single particle images with randomly distributed positions and sizes. The particles have diameters in the range of $d_P = [20, 300]$ µm and a random distance from the focal plane in the range of $z_P = [1, 8]$ mm. The in-plane position was randomly generated for the PI to be still fully within the image. The pixel accuracy is shown as the black dashed line, and the micro-meter accuracy (for the present optical system) as a red dashed line.

Table 1. Median Error for 200 synthetic PIs with random particle parameters ψ_P. The particles have diameters in the range of $d_P = [20, 300]$ µm and a random distance from the focal plane in the range of $z_P = [1, 8]$ mm. For the FFT approach a random error within an uncertainty of $\Delta x_{PI}, \Delta y_{PI}, \Delta d_{PI} = 1$ px was added to the ground truth parameters ψ_P. The FFT was then performed on the initialized value. For the InvP approach a random placement error for the BB $\Delta x_{PI}, \Delta y_{PI}, \Delta d_{PI} = 1$ px and 5 px was used to initialize the starting values of the optimization. The factor of improvement for the InvP based on the chosen FFT+BB (with 1 px error) approach is given in the last two lines of the table. The improvement factor of the InvP with 5 px initialization error relates to an improvement over the FFT+BB with 1 px error.

	median error in µm			median Error	in pixel
Method	(x_P, y_P) (µm)	z_P (µm)	d_P (µm)	(x_P, y_P) [px]	z_P [px]
FFT + BB (1 px)	(6.45, 6.45)	81.4	47.2	(1,1)	1
InvP (1 px)	(2.43, 0.38)	3.13	0.16	(0.38,0.06)	0.04
InvP (5 px)	(3.65, 0.47)	42.4	0.85	(0.57,0.07)	0.52
improvement factor InvP (1 px)	(2.6, 17.0)	26.0	295	–	–
improvement factor InvP (5 px)	(1.8, 13.7)	1.9	55.5	–	–

effect was, however, not observed when optimizing over multiple particles, see section 5.2 and is seems to become irrelevant in case of higher dimensional spaces. The in-plane accuracy of the InvP approach is comparable to current bench marks in DPTV such as the cross correlation approach [50] and the

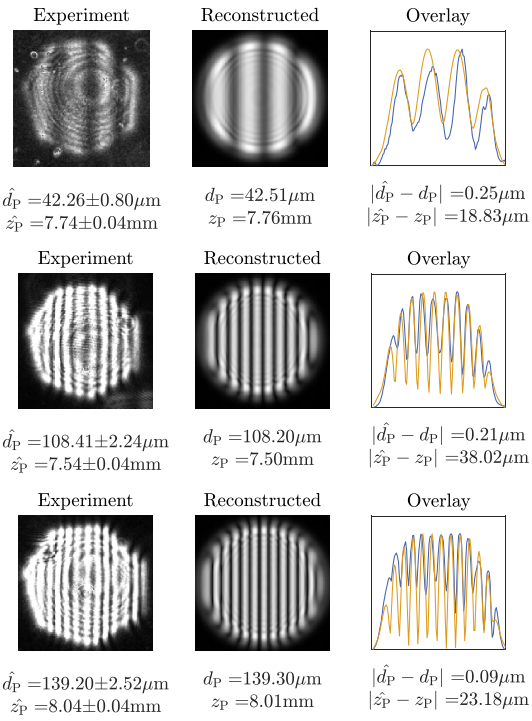

Figure 15. Real PIs from the bubble experiment [23] (left), the PI from the InvP result (middle) and the image overlay (right) (observed—blue channel; InvP—red channel). Given are the ground truth values $\hat{z_P}, \hat{d_P}$ (i.e. measurement with conventional approach) with the measurement uncertainty (left), the values obtained from the InvP approach z_P, d_P (middle) and the discrepancy of the two methods (right). The same images as in figure 9 for the validation of the FM were used. Similar to figure 9, the blue line on the right represents the experiment and the orange line, the reconstruction by the IP.

circular Hough transform [51]. A poor initialization has only little effect on the in-plane position estimation, due to the smoothness of the mismatch functional for a single PI in x and y direction. For the z-position accuracy, a significant improvement over pixel accuracy is achieved, with the error being in the same-order of magnitude as the in-plane error. The effect is less pronounced for a poor initialization but still significantly better than pixel accuracy. However, this effect might not hold for the application on real images due to differences in the aperture shape between simulation and real experiment. The biggest improvement of the InvP approach is in the estimation of particle diameter d_P. As the FFT approach is reliant on a known z-position, even small errors in the z position cause large deviations in the diameter estimation as the error propagates linearly onto the diameter estimation, compare equation (1). This is not the case for the InvP approach and even for a poor initialization (± 5 px) sub-micrometre accuracy is achieved. The correlation between the z-position and diameter errors is 0.06. Even for a less accurate z position (42.4 µm), as is the case for the poor initialization, remains the diameter estimation largely unaffected (0.86 µm). The uncorrelated diameter estimation poses an improvement of the diameter estimation of more than two orders of magnitude for single PIs.

4.4. Transferability to real particle images and robustness of InvP approach

For synthetic PIs the InvP approach shows some improvement of accuracy over the FFT approach. However, the InvP approach takes advantage from using the same FM as the synthetic observed images. Therefore, the transferability of these results to real images needs to be investigated.

To test this the same PIs used for the validation of the FM, see figure 9, are used. The InvP approach is applied to the real images, using an initialization from BBs with a placement accuracy of $\Delta x_{PI}, \Delta y_{PI}, \Delta d_{PI} = \pm 1$ px.

The result of the optimization can be seen in figure 15. For all three particles the InvP approach returns a result within the measurement uncertainty of the FFT + BB (1 px uncertainty) approach. The amount of improvement of estimation accuracy, can however not be quantified, since the ground truth bubble position and diameter is subject of the uncertainty of the conventional measurement method (FFT + BB) and therefore not known with higher accuracy. With the InvP approach, a distinct minimum for ψ_P is found within the uncertainty of the FFT + BB approach. This means that the InvP approach is at least as accurate on real data as the FFT + BB approach. The higher accuracy on synthetic data (see section 4.3) and the distinction of the minimum within the uncertainty of the

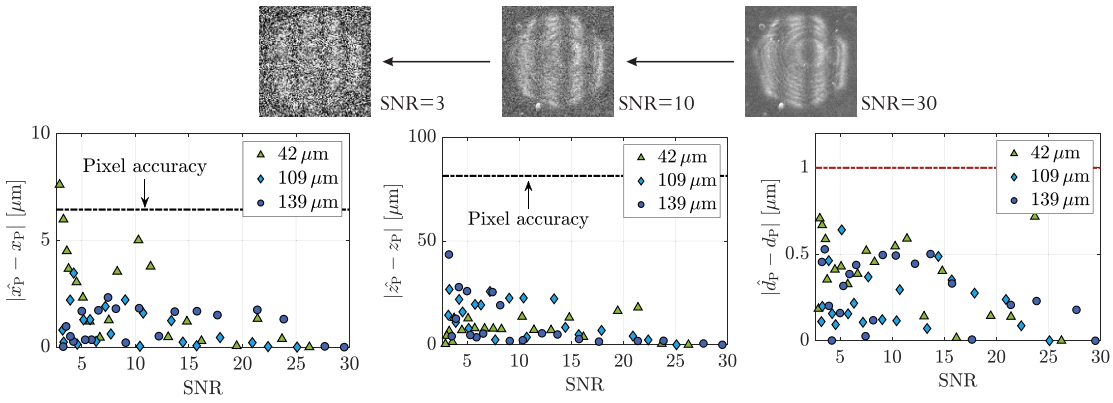

Figure 16. Consistency of the InvP approach for images with increased noise levels. Images from the bubble experiment were used and Gaussian noise was added to decrease the SNR (top). The change of the optimization result of the InvP approach for different noise levels is shown for the x-position (left), the z-position (middle) and the diameter (right). The values $(\hat{x_\mathrm{P}}, \hat{z_\mathrm{P}}, \hat{d_\mathrm{P}})$ refer to the results of the InvP approach without added noise, see figure 15. The error is the deviation from the 'noise free' results. The same images as in figure 9 for the validation of the FM were used.

FFT + BB approach suggest, that the InvP approach is considerably more accurate than the FFT + BB approach. Due to the unknown ground truth, however, this improvement is difficult to quantify. The InvP approach also achieves sub-micrometre accuracy (for the given optical system) for the diameter even in the case of an unknown z-position, and sub-pixel accuracy of the z-position despite the mismatch of the heptagonal aperture with the assumed circular one in the FM. It is likely that a heptagonal aperture function would further increase the z-position accuracy of the InvP approach, but would render the approach less flexible to optical systems with other apertures.

A common issue in IPI is low signal-to-noise ratio (SNR) as occurs for large defocus distances, compare figure 7, small particles and measurement at certain scattering angles [23]. To test the InvP approach for the robustness against low SNR, the same images as used in figures 9 and 15 are used, with white Gaussian noise added to decrease the SNR post-measurement. The original images all had an SNR larger than 30 and noise was systematically added until the SNR was lowered to 2.6, compare figure 16. The SNR was defined as the average intensity of the peaks in the fringe pattern (i.e. stripes) compared to the variance of the background. Variance is commonly used to quantify noise power independently of shifts in background intensity, particularly under the assumption of Gaussian-distributed noise, which is a standard model for image noise. Since the ground truth of the bubbles in the real experimental images is only known with the uncertainty of the FFT + BB approach, the error with increasing noise is quantified by the consistency of the InvP approach returning the same result for ψ_P despite the added presence of noise. The accuracy reference $(\hat{x_\mathrm{P}}, \hat{y_\mathrm{P}}, \hat{z_\mathrm{P}}, \hat{d_\mathrm{P}})$ is therefore the result returned by the InvP approach for the original image (without added noise, SNR>30). The error stemming from added noise is then defined as the difference of the returned values of the InvP on images with noise $(x_\mathrm{P}, y_\mathrm{P}, z_\mathrm{P}, d_\mathrm{P})$ from the values of the InvP on the original images.

The results are shown in figure 16, which outlines that all dimensions of optimization behave very similar in the presence of noise. For higher SNR levels almost no influence of noise is observed for the 3D localization, while for extremely low SNR levels of close to 2.6, the returned result starts to vary more significantly. A closer look at the topology of the mismatch-functional reveals that the smoothness of the optimization landscape is barely affected by the noise, but the global minimum experiences a small shift due to the noise. This reveals that the influence of noise on the InvP is an issue affecting the mismatch functional and is, therefore, not an FM or solver-related issue. The increased variance of ψ_P in the presence of noise can therefore, be explained by noise introduced shifts of the global minimum. However, despite very low SNR, the returned result stays sub-pixel accurate for the position and sub-micrometre accurate for the particle diameter determination.

5. IP for multiple particles

The last section demonstrated the feasibility of the InvP approach for single particles and suggests improvements in measurement accuracy and noise resistance compared to current benchmark approaches. Almost all measurement scenarios, however, involve multiple particles. In such multi-particle systems, the PIs must be considered together, as the PI overlap in turn leads to superimposed patterns.

These overlap regions of the PIs, affected by the superposition, can become complex as multiple fringe frequencies and orientation of the fringes can occur. To accurately fit a PI onto another PI, the other PI's parameter must be known beforehand. Therefore, the InvP approach for multiple particles optimizes all particles in the same image at once. Similar to the single particle approach, machine learning techniques for object detection can again be used to place BBs around every PI to provide starting points for the x, y, z positions of each particle.

5.1. Mismatch functionals and optimization

To fit all particles in the image at once, the particle parameter vector is extended to

$$\psi_{\mathrm{I}} = (\underbrace{x_{\mathrm{P},1}, y_{\mathrm{P},1}, z_{\mathrm{P},1}, d_{\mathrm{P},1}}_{\textbf{particle 1}}, \underbrace{x_{\mathrm{P},2}, y_{\mathrm{P},2}, z_{\mathrm{P},2}, d_{\mathrm{P},2}}_{\textbf{particle 2}}, \ldots, \underbrace{x_{\mathrm{P,N}}, y_{\mathrm{P,N}}, z_{\mathrm{P,N}}, d_{\mathrm{P,N}}}_{\textbf{particle } N})^{\mathrm{T}} \tag{30}$$

with the length $4N$ for N particles in the image ($\psi_{\mathrm{I}} = (\psi_{\mathrm{P},1}^{\mathrm{T}}, \psi_{\mathrm{P},2}^{\mathrm{T}}, \ldots, \psi_{\mathrm{P},\ell}^{\mathrm{T}}, \ldots, \psi_{\mathrm{P},N}^{\mathrm{T}})^{\mathrm{T}}$). The image G_{image} is then computed from the complex fields $G_{2,\ell}$ of the individual particles ℓ using equation (24). The number N of particles in the image is assumed to be known and can be retrieved from a particle detection algorithm (i.e. number of BBs in the image), compare the initialization scheme in figure 11. While, there is a lot of research (e.g. [12, 13, 16]) published on the position accuracy of neural networks, only few papers discuss the detection rate [14, 15, 52, 53]. However, recent approaches for particle detection algorithms have shown to have sufficiently low miss rates to initialize an InvP approach. To deal with the many local minima in this high dimensional space, again the initialization based on the BBs $(x_{\mathrm{PI},\ell}, y_{\mathrm{PI},\ell}, d_{\mathrm{PI},\ell})$ of each PI_ℓ is used to obtain good starting values for the optimization.

The optimization routine remains identical to the single particle optimization: first the positions are optimized and in the second step the z-positions and the diameters are refined. In the first step the full vector ψ_{I} is fitted in order to identify the individual particle positions and the diameter is again kept as a free parameter in order to adapt the PI shapes. To suppress interference in this step the image is computed from

$$G_{\mathrm{image,pos}} = \sum_{\ell=1}^{N_{\mathrm{P}}} G_{\mathrm{P,pos},\ell} = \sum_{\ell=1}^{N_{\mathrm{P}}} |G_{2,\ell,\mathrm{GP1}}| + |G_{2,\ell,\mathrm{GP2}}| \tag{31}$$

for N_{P} particles. The mismatch functional $\mathcal{P}_{\mathrm{I,pos}}$ is then computed identical to the single particle approach ($\mathcal{P}_{\mathrm{P,pos}}$), compare equation (28). To compute the mismatch functional for the diameter, the PIs are Fourier-transformed individually. For this, an image snippet of each particle ℓ is used for the mismatch functional. The image snippet is computed from a BB, of which the centre is derived from $x_{\mathrm{P},\ell}, y_{\mathrm{P},\ell}$ and the BB diameter is derived from $z_{\mathrm{P},\ell}$ and equation (4). The mismatch functional $\mathcal{P}_{\mathrm{I,dia}}$ is then computed from the individual Fourier-transformed image snippets and takes the form of

$$\mathcal{P}_{\mathrm{I,dia}} = -\frac{1}{N} \sum_{\ell=1}^{N} \left(\mathcal{F}_2 \{ G_{\mathrm{PI},\ell} \} \star \mathcal{F}_2 \{ G_{\mathrm{PI,ref},\ell} \} \right), \tag{32}$$

which is an expansion of equation (29). To initialize the diameters, again a global search is run over the individual PIs using equation (29). In the second step the local search again only optimizes the z-positions and diameters so that the optimization vector in the second step takes the form of

$$\psi_{\mathrm{I,zd}} = \left(\underbrace{z_{\mathrm{P},1}, d_{\mathrm{P},1}}_{\textbf{particle 1}}, \underbrace{z_{\mathrm{P},2}, d_{\mathrm{P},2}}_{\textbf{particle 2}}, \ldots, \underbrace{z_{\mathrm{P,N}}, d_{\mathrm{P,N}}}_{\textbf{particle } N} \right)^{\mathrm{T}} \tag{33}$$

and has the size of $2N$. Since the z-positions and diameters of the particles are optimized together, the objective functional of the second step takes again the form of $\mathcal{P}_{\mathrm{I}} = \mathcal{P}_{\mathrm{I,dia}} + \mathcal{P}_{\mathrm{I,pos}}$, similar to the single particle approach. The approach for multiple particles is essentially identical to the single particle approach, but the generated images contain multiple PIs.

The multi-particle InvP approach has the following advantages: The shape of overlapping PIs and the super-positioned fringe pattern can be accurately represented by the FM. The LMT-DSE model in the FM intrinsically models changes in intensity with varying particle size and scattering angle (i.e. x, y position of particle). Also the intensity change with the z-position is accounted for, which is indicated by the intensity loss in figure 7. The increased intensity and varied interference pattern in overlapped parts

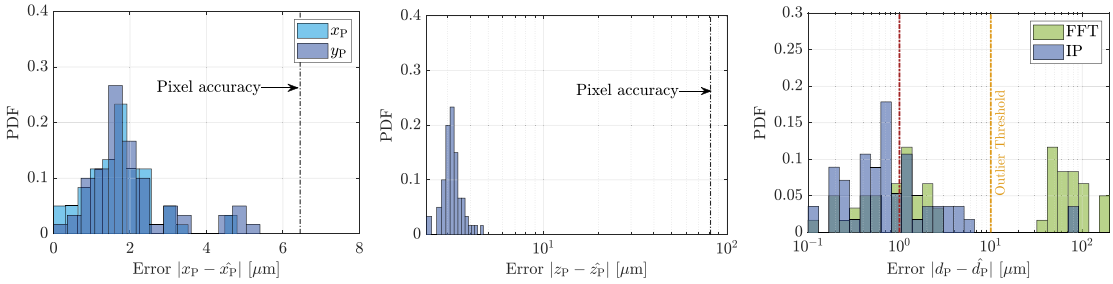

(a) In-plane error (b) Out-of-plane error (c) Diameter error

Figure 17. Probability density functions for the in plane x and y errors (a), the out-of-plane errors (b) and the diameter estimation error (c). For the diameter error also the FFT approach is plotted as comparison. Similarly to the FFT, the InvP approach was initialized with 1 px uncertainty. Ten images with 20 particles each where generated with random particle parameters in $d_P \in [20\,300]$ µm and $z_P \in [1, 8]$ mm. The pixel accuracy is shown as the black dashed line, and the micro-meter accuracy as a red dashed line. The yellow dashed line in (c) marks the threshold beyond which outliers are defined.

between PIs is also accounted for by the FM as the complex fields of the PIs are superimposed. These characteristics let the approach use the relative intensity between PIs as an additional feature, which other approaches do not take advantage of.

5.2. Tests on synthetic data

To test the multi-particle InvP approach, again synthetic images are generated with the FM to have a ground truth for the analysis. Similar to the single particle tests, noise is added to the observed images and the optimization is initialized from BBs with ± 1 px and ± 5 px placement uncertainty (random derivations for each BB $\Delta x_{PI}, \Delta x_{PI}, \Delta x_{PI} \in [-5, 5]$ or $[-1, 1]$). For comparison, also the FFT + BB (± 1 px uncertainty) approach is applied to the images. The random initialization for the FFT + BB approach and for the InvP approach where exactly the same (for the InvP approach multiplied by 5 in case of the ± 5 px initialization) to cancel out the influence of 'lucky' placements of BBs. Ten different images containing 20 particles each were generated for testing.

The results of the test are shown in figure 17. It can be seen that the multi-particle InvP approach remains sub-pixel accurate in the in-plane position for a good initialization, but not for a poor initialization (± 5 px), see the improvement factors in table 2. This is due to the non-smooth landscape of the optimization function, where the optimization gets stuck in a local minimum, if not initialized properly. In the case of a poor initialization (± 5 px) the in-plane error is still reduced from the BB error of 32.25 µm to 10.5 µm, which poses an improvement by the factor of 3. The z-position error remains almost identical for the multi-particle approach (3.13 vs 3.15 µm error for the good initialization and 42.4 vs. 61.8 µm for the poor initialization). The landscape of the mismatch-functional is mostly convex in the z dimension for single particles and is also smoother than in the x, y dimensions for multi-particle systems. The InvP approach improves the particle parameter compared to its initialization significantly even for a poor initialization. For the diameter estimation also similar results to the single particle approach are achieved. The InvP approach achieves significantly better results in the diameter estimation due to the uncorrelated diameter and z position determination. The investigation of the diameter error shows that the error probability density function (pdf) is split into two parts. An arbitrary threshold of a diameter error of the order of magnitude of 10 µm and above is defined to mark outliers in the estimation, based on the separation of the two pdfs, compare figure 17(c). The number of outliers is significantly reduced with the InvP approach compared to the FFT+BB approach (25 to 5). It should be noted that, without the significant number of outliers, the diameter uncertainty of the unaffected particles (left peak in the PDF) in the case of a sequential approach (i.e. ignoring the right peak) is comparable between the FFT and InvP approaches. This again highlights the effect of error propagation from the z-position into the diameter estimation.

5.3. Particle image overlap

As the InvP approach achieves very similar results for multiple particles compared to single particles, the effect of PI overlaps on the result is investigated in more detail. To investigate the influence of PI overlaps in images with multiple particles, the cumulated intersection over area (IoA) of each PI is defined. The IoA describes the amount of overlap between two objects in relation to the area of the considered PI. It therefore shows the fraction of an individual PIs area that is covered by another particle. The IoA

Table 2. Median errors of the FFT + BB (1 px uncertainty) and the InvP approach (initialization with 1 px and 5 px uncertainty). The factor of improvement of the result using the InvP approach is given below. The number of outlier is stated, with an outlier, arbitrarily being defined as an error in diameter of more than 10 µm. The outlier threshold of 10 µm was chosen based on the PDFs in figure 17(c), where two ranges of high probability are separated: one in the order of magnitude of 1 µm and the other in the order of magnitude of 100 µm. The improvement factor of the InvP with 5 px initialization error relates to an improvement over the FFT+BB with 1 px error. Note that the values for x_P, y_P, z_P for the BB approach represent pixel accuracy and are imposed errors. The error of d_P is the resulting error from a measurement with an FFT + a 1px uncertainty in the z-position.

	median error			number of outliers
Method	(x_P, y_P) (µm)	z_P (µm)	d_P (µm)	$(\lvert\hat{d_P} - d_P\rvert > 10\,\mu m)$
FFT + BB (±1 px)	(6.45, 6.45)	81.4	34.4	25
InvP (±1 px)	(1.68, 1.77)	3.15	0.72	5
InvP (±5 px)	(10.5, 14,4)	61.8	2.81	10
improvement factor InvP				
(initialization ±1 px)	(3.8, 3.6)	25.8	47.7	5
(initialization ±5 px)	(0.61, 0.44)	1.3	12.2	2.5

is introduced as

$$\mathrm{IoA}_{\ell,j} = \frac{A_{\mathrm{PI},\ell} \cap A_{\mathrm{PI},j}}{A_{\mathrm{PI},\ell}}. \tag{34}$$

with $A_{\mathrm{PI},\ell}$ being the area of the PI. The cumulated IoA for a particle ℓ sums up the IoA of the PI ℓ with every other PI j in the image

$$\text{cumulated IoA}_\ell = \sum_j \mathrm{IoA}_{\ell,j} \tag{35}$$

and, therefore, provides a measure for the total amount of area in the PI that is covered up by overlap. Figure 18(a) shows the z-error for each PI in relation to the cumulated IoA. From figure 18(a), it can directly be seen that the z-error is unaffected by the overlap. The same goes for the diameter error as can be seen in figure 18(b). The comparison between the FFT and the InvP approach, both for ±1 px BB placement accuracy, reveals that the InvP approach produces significantly less outliers and achieves consistently lower errors in the presence of strong overlaps. To visualize the performance of the FFT+BB approach compared to the InvP approach, figure 19 shows two of the test images with the respective error category (< 1, $[1, 10]$ and > 10 µm error). It can be seen that the FFT approach (fitting a single peak in frequency space) works well for non-overlapping PIs but creates a significant amount of outliers in the presence of even small PI overlaps. The FFT approach results in large errors even for small amounts of overlap. This is due to the presence of other significant peaks in the Fourier space due to the superposition of frequencies. Consequently, any of the frequencies might be detected and it is difficult to identify the correct one. For the InvP approach on the other side, most particles could be reconstructed despite larger PI overlaps. The number of outliers in the presence of overlaps is reduced from 25 (FFT) to 5 with the InvP approach. However, the InvP approach still produces some outliers. These outlier PIs were all significantly less bright than the other PIs surrounding them, indicating that the intensity of PIs does have an important role on the reconstruction. This is likely due to brighter PIs influencing the mismatch functional more than dimmer ones. PIs less bright than their surrounding PIs stem either from smaller particles or more defocused particles. This means that these two types of particles are most likely to be wrongly reconstructed. Considering the many outliers caused by PI overlaps when using the FFT approach, the InvP approach yields a promising alternative for the improvement of median and mean accuracy in diameter estimation. However, the InvP approach also returns larger errors on PIs, which are isolated from other PIs without any overlap. This stems from the challenging topology of the mismatch-functional.

5.4. Particle reconstruction from the InvP approach

Finally, the InvP approach is used to reconstruct a full three dimensional particle field, from the (synthetic) observed image. For the visualization of the application, one of the ten test images from section 5.2 is chosen. Figure 20 shows the ground truth particle field with the three dimensional positions and diameters, that was used to generate the observed image with the FM. The reconstructed particle field is shown next to the ground truth. It can be seen that all but one particle were reconstructed with sufficient accuracy. The position of this one particle was still reconstructed correctly and only the diameter was estimated wrongly. Finally, figure 21 shows the application of the InvP approach on a

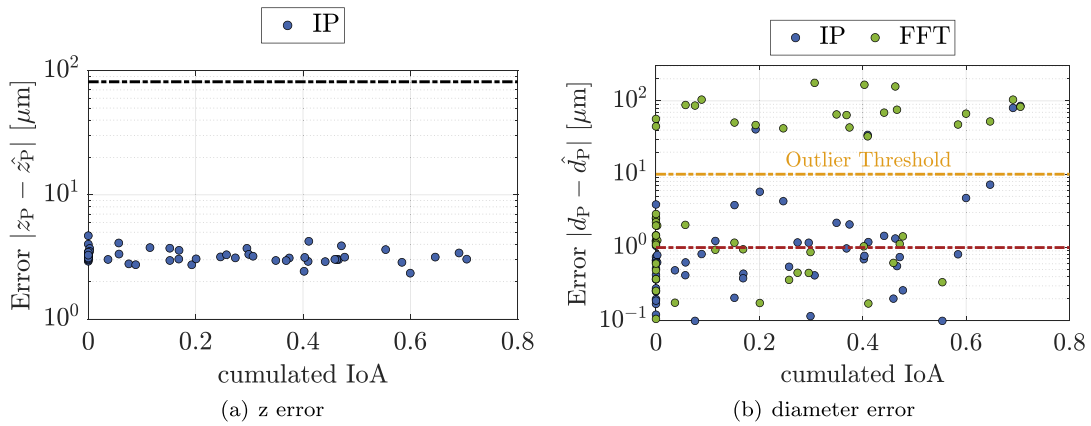

Figure 18. The z-position (a) and diameter (b) errors over the cumulated Intersection over area (IoA) of the PIs. The IoA is the intersection area of a PI divided by its area. The accumulated IoA is the summed IoA of a PI with all other PI overlaps and shows the amount of the PI area that is overlapped. In (a) the dashed black line represents the pixel accuracy. In (b) the thresholds of a 1µm diameter error (red line) and for the outlier definition of an error of 10µm (yellow line) are visualized. The errors are shown for the InvP approach and for the FFT approach both with a 1 px BB accuracy for initialization. The FFT approach and the InvP approach are initialized from a ± 1 px BB placement accuracy.

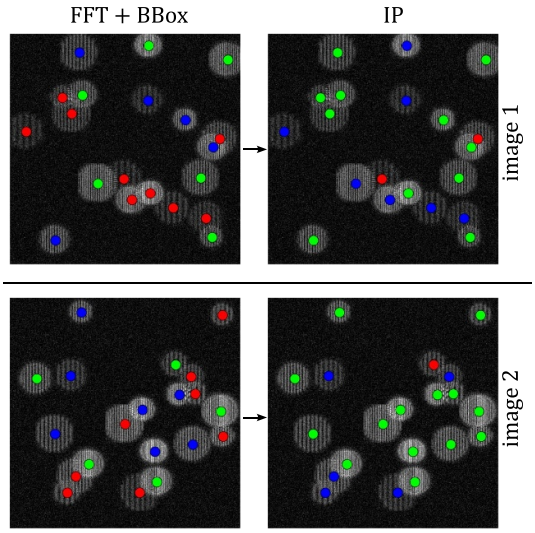

Figure 19. The estimation results of two of the 10 synthetic test images visualized for the FFT + BB (1 px placement uncertainty) and the InvP approach. A coloured dot is added on each PI to show the error of the diameter determination: For an error < 1 µm a green dot is placed (•), for an error in $[1, 10]$ µm a blue dot (•) and for outlier particles (error > 10 µm) a red dot is placed (•). The seeding density in the images is given by $\mathcal{S} = \sum_i \frac{\pi}{4} d_{\mathrm{PI},i}^2 / A_{\mathrm{image}} = 0.27$, following the definition by Barnkob & Rossi [54], which relates the defocused PI area to the image area A_{image}.

real image from the bubble experiment [23], which was also used to validate the FM in figure 9, with multiple particles. The InvP approach finds the particle parameters ψ_I that result in a good agreement of the observed image with the reconstructed image according the mismatch functional $\mathcal{P}$. For a qualitative check of the reconstruction, the reconstructed image, based on the determined ψ_I, can be generated using the FM. A visual comparison shows great agreement between the experimental image and the reconstructed image. The particle field is then directly obtained from the particle parameter vector ψ_I.

6. Discussion and conclusions

There are several challenges in DPTV and IPI that the proposed InvP approach aims to address. The first is the out-of-plane accuracy in DPTV, which is usually an order of magnitude lower than the estimation of the in-plane position. PI overlaps furthermore present a limit to the number of particles that can be evaluated, the maximum defocus length and defocus sensitivity, as well as the spatial resolution of fringes in IPI. Moreover, the coupling of the z-position with the diameter estimation present an issue

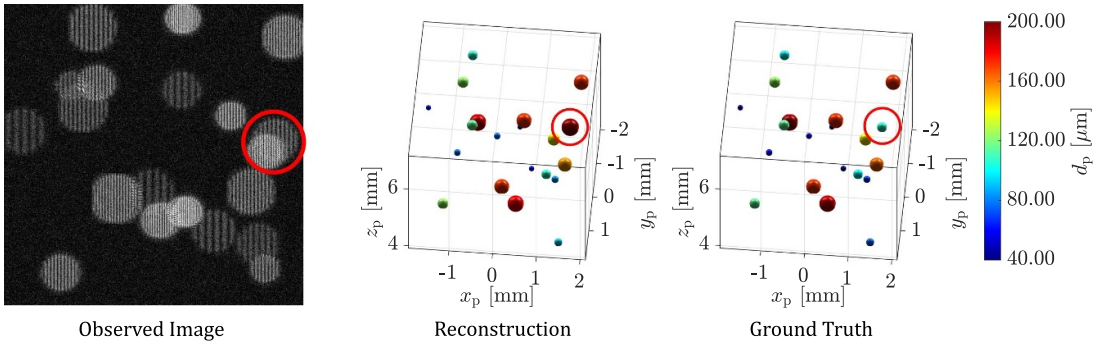

Figure 20. Synthetic observed image and the reconstruction by the InvP approach visualized. The reconstructed particles are compared to the ground truth used to generate the observed image. In the present example, one particle was reconstructed with a false diameter but correct position, and is marked by the red circle. The seeding density in the images is given by $\mathcal{S} = \sum_i \frac{\pi}{4} d_{\mathrm{PI},i}^2 / A_{\mathrm{image}} = 0.27$, following the definition by Barnkob & Rossi [54], which relates the defocused PI area to the image area A_{image}.

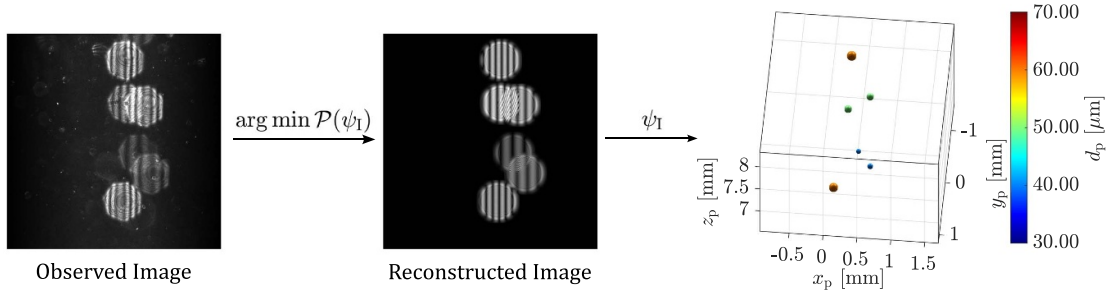

Figure 21. Example of the use of the InvP approach on real experimental data. The observed image is from the bubble experiment. The observed image is fitted by minimizing the mismatch functional $\mathcal{P}$. The FM is used to generate an image with the optimal particle parameter set ψ_I. This image can be used as a reference to qualitatively check the result of the InvP approach. The particle positions and diameters are then directly obtained from ψ_I.

in IPI for the sizing of 3D distributed particles. Lastly, aliasing presents a lower limit on defocusing and upper limit on the particle size in IPI.

The inclusion of an FM in the IPI measurement offers several advantages: It allows an approach to use the relative intensity of PIs as an additional feature to extract information. Effects such as changing intensity due to particle size, z-position and scattering angle (x, y-position) [23] are taken into account by the FM, which would otherwise have to be considered manually. This is particularly important for IPI in side- and backscatter where large intensity variations can occur. Note that the present manuscript used images from the experiment described by Sax *et al* [23] for performance evaluation. Accordingly, the absolute errors discussed in this manuscript are subject to the underlying optical system used in the experiment and may change for other setups. However, while the overall accuracy of the particle parameter estimation scales with the optical transfer function, the relative improvements between the approaches are expected to persist across different experimental setups.

The InvP approach showed to have a z-position accuracy in the same order of magnitude as the in-plane position on synthetic data. A similar trend was observed on real data, however the exacted uncertainty on real data is difficult to quantify. The InvP approach, therefore poses a promising counteraction to large out-of-plane uncertainties in the 3D position determination with a single camera by means of defocusing.

Aliasing effects of the fringe pattern can also be taken into account. There are two ways aliasing can occur, by either large particles or by particles close to the focal plane, see figure 10. According to equation (1) and B_{tot} being linearly depended on z_p, is the Pareto front of occurring aliasing linear. Therefore, an increase in d_p must be compensated by a linear increase in z_p to avoid aliasing. While conventional FFT based approaches are limited by aliasing, the InvP approach can operate beyond the point of aliasing (decreased z_p for a given particle size d_p). As a result, the focal plane can be moved closer to the particles in the measurement, resulting in less overlap and higher intensities (i.e. higher SNR). This is a significant advantage over non-FM approaches as the quality of the raw data can be

improved by imaging closer to the focal plane. This is particularly important for measurements in the side- and backscatter regions, which generally suffer from low SNR [23]. The approach presented, therefore, addresses one of the most important issues in backscatter IPI. In addition, the InvP approach shows great resilience to the presence of noise, to the point where most particle detection methods fail. The ability of the InvP approach to deal with low SNR levels (e.g. from particles further away from the focal plane) and aliasing (e.g. from particles closer to the focal plane) allows the measurement volume in the z dimension to be extended in both directions. Consequently, potentially deeper volumes can be measured with the InvP approach compared to other methods. Alternatively, this characteristic of the InvP approach can also be used to allow for the use of optical systems with higher defocusing sensitivity (larger change in d_{PI} with z_{P}) to further increase the z-position accuracy.

Comparisons with the FFT+BB approach show that the InvP approach is at least as accurate as the current benchmark on real data with sub-micron accuracy in diameter measurement for the optical setup in this work. The InvP approach has another significant advantage over the FFT approach in that the z position and the diameter estimation are decoupled. This results in significantly higher diameter accuracy for three dimensionally distributed particles, as the error in the z-position estimation does not propagate into the diameter estimation. This feature makes the InvP approach more accurate than sequential approaches that first determine the z-position of a particle and then use this estimate to calculate the diameter. The InvP approach presented in this work introduces a competitive approach for the simultaneous position and size determination of three-dimensionally distributed particles, alongside currently existing approaches such as IPI+APTV approaches [20, 21, 55] and InvP in holography [24, 25]. The presented InvP approach can be applied to systems with optical elements such as lenses, apertures and glass walls, which are challenging for holographic approaches. The approach can also be used to size both droplets and bubbles, as the scattering model takes into account the different scattering process for any real-valued relative refractive index.

The InvP approach can be extended to measure multiple particles simultaneously. The main problem in multi-particle systems is PI overlap, which causes approaches that rely solely on frequency extraction (either by FFT or counting fringes) to produce erroneous estimations due to the presence of other frequencies caused by the superposition of PIs. The InvP approach, however, is largely unaffected by PI overlap. The approach, therefore, addresses the PI overlap problem in both DPTV and three-dimensional IPI. The InvP approach, therefore, relaxes the trade-off between the need for larger PIs to improve fringe resolution (and avoid aliasing) and the need for smaller PIs to reduce PI overlap [22]. Another factor affecting this trade-off is the need for high SNR, which again makes small PIs advantageous. With a high noise resistance and intensity as an additional feature in the FM, can the InvP approach also deal with larger defocused PI with lower SNR, and, therefore, partially mitigates this part of the trade-off as well.

While the InvP approach offers advances in many of the key challenges in DPTV and IPI, the accuracy of the approach is mainly limited by the accuracy of the used FM and the used optimization scheme. As the mismatch-functional is non-convex and the dimensionality of the problem is too high for a global optimization, a local search faces the challenge of terminating in a local minimum. These minima are often sufficiently close to the global minimum, so that the particle parameters are approximated with great accuracy, as shown in the present work. With an increased number of particles in the measurement volume, the higher dimensionality introduces more local minima. This is a crucial insight, as the accuracy at which a PI is reconstructed does not depend of the PI overlap, but is rather subject to which local minimum the solver terminates in. This also shows the importance of good initialization. For a different initialization, therefore, a slightly different result is expected. This can be used to run an ensemble method (multiple optimization runs with random perturbations in initialization) on the same image to provide a measure of uncertainty for real experimental approaches.

The presented InvP approach poses a promising method to refine detections from machine learning methods as conceptualized in the hybrid approaches [15]. While the InvP approach results in larger computational cost compared to FFT approaches for sizing or a Hough transform for the position determination, the method may be used for off-line measurements to improve accuracy, where the time to results is not of the essence.

In comparison to other methods—such as sequential approaches utilizing APTV or DPTV for position determination and FFT, sine fit, or stripe counting for diameter estimation—the InvP approach offers several key advantages: it decouples the z-position and diameter estimation, is robust to PI overlap, and can effectively handle aliasing. These characteristics enable a level of measurement accuracy that is difficult to achieve with conventional methods. On the other hand, the InvP approach comes with drawbacks, including increased computational time and sensitivity to initialization. The computational cost of the FM scales as $\mathcal{O}(n)$, with n being the number of particles in the image. However, the optimization required to minimize $\mathcal{P}$ typically scales polynomially, and runtime may increase super-linearly

depending on the chosen optimizer. For n particles, a $4n$-dimensional minimization problem with box constraints must be solved. As the scaling also depends on the sparsity of the Hessian, it can be expected that the block corresponding to each individual particle is dense, while the overall Hessian—composed of mostly diagonal particle blocks—remains sparse, assuming particles are independent. However, with increasing PI overlap, inter-particle dependencies grow, making the Hessian more dense and potentially degrading runtime behaviour. Additionally, non-convexity can further increase runtime and contributes to sensitivity to initialization accuracy. Beyond initialization, undetected particles in the detection step can cause a mismatch between the observed and simulated image, potentially leading the optimizer to terminate in a suboptimal solution. A possible workaround is particle detection via optimization, as demonstrated by Soulez *et al* [25], though this would further increase computational complexity.

The next development step for the InvP approach would be to use the approach for two-phase flows, as different kinds of particles such as single emitters (e.g. tracers) and double emitters (bubbles/droplets) can easily be represented within the present approach (i.e. by omitting the diameter parameter for tracers). The capability of the InvP approach to deal with low SNRs and tolerate aliasing when imaging particles closer to the focal plane to obtain better SNR, can improve the evaluation of data with poor quality. In consequence, this presents a promising step towards IPI in backscatter, which is suffering from poor data quality. Future steps could also include more complex particles such as multi-emitters like those arising from rough particles [56] or non-circular bubbles and droplets [57, 58].

Data availability statement

The data that support the findings of this study are openly available at the following URL/DOI: https://doi.org/10.1103/7kc3-7yyh.

Acknowledgments

This work was supported by the Deutsche Forschungsgemeinschaft (DFG, German Research Foundation) via Project Grant KR4775/4-1 within the Research Unit FOR 5595 Archimedes (Oil-refrigerant multiphase flows in gaps with moving boundaries—Novel microscopic and macroscopic approaches for experiment, modeling, and simulation)—Project Number 510921053.

Author contributions

Christian Sax 0000-0003-0749-224X
Conceptualization (equal), Data curation (lead), Formal analysis (equal), Investigation (lead), Methodology (equal), Software (lead), Validation (equal), Visualization (lead), Writing – original draft (lead), Writing – review & editing (equal)

Roland Griesmaier 0000-0002-1621-6127
Conceptualization (equal), Formal analysis (equal), Methodology (equal), Supervision (equal), Validation (equal), Writing – review & editing (equal)

Jochen Kriegseis 0000-0002-2737-2539
Conceptualization (equal), Formal analysis (equal), Funding acquisition (lead), Project administration (lead), Supervision (equal), Validation (equal), Writing – review & editing (equal)

References

[1] König G, Anders K and Frohn A 1986 A new light-scattering technique to measure the diameter of periodically generated moving droplets *J. Aerosol Sci.* **17** 157–67
[2] Niwa Y, Kamiya Y, Kawaguchi T and Maeda M 2000 Bubble sizing by interferometric laser imaging *10th Int. Symp. on Application of Laser Techniques to Fluid Mechanics*
[3] Kim D, Schanz D, Novara M, Seo H, Kim Y, Schröder A and Kim K C 2022 Experimental study of turbulent bubbly jet. part 1. simultaneous measurement of three-dimensional velocity fields of bubbles and water *J. Fluid Mech.* **941** A42
[4] Wang L, Ma T, Lucas D, Eckert K and Hessenkemper H 2025 A contribution to 3D tracking of deformable bubbles in swarms using temporal information *Exp. Fluids* **66** 34
[5] Kao H P and Verkman A S 1994 Tracking of single fluorescent particles in three dimensions: use of cylindrical optics to encode particle position *Biophys. J.* **67** 1291–300
[6] Willert C E and Gharib M 1992 Three-dimensional particle imaging with a single camera *Exp. Fluids* **12** 353–8
[7] Fuchs T, Hain R and Kähler C J 2016 In situ calibrated defocusing PTV for wall-bounded measurement volumes *Meas. Sci. Technol.* **27** 084005
[8] Bryanston-Cross P J, Funes-Gallanzi M, Quan C and Judge T R 1992 Holographic particle image velocimetry (HPIV) *Opt. Laser Technol.* **24** 251–6

[9] Leister R, Fuchs T and Kriegseis J 2023 Defocusing PTV applied to an open wet clutch: from macro to micro *Exp. Fluids* **64** 94
[10] Lecun Y, Boser B, Denker J, Henderson D, Howard R, Wayne H and Jackel L 1990 Handwritten digit recognition with a back-propagation network *Advances in Neural Information Processing Systems (NeurIPS)* vol 2 (https://proceedings.neurips.cc/paper/1989/file/53c3bce66e43be4f209556518c2fcb54-paper.pdf)
[11] Lecun Y, Bottou L, Bengio Y and Haffner P 1998 Gradient-based learning applied to document recognition *Proc. IEEE* **86** 2278–324
[12] Cierpka C, König J, Chen M, Boho D and Mäder P 2019 On the use of machine learning algorithms for the calibration of astigmatism PTV *Proc. 13th Int. Symp. on Particle Image Velocimetry (PIV19)*
[13] Franchini S and Krevor S 2020 Cut, overlap and locate: a deep learning approach for the 3d localization of particles in astigmatic optical setups *Exp. Fluids* **61** 140
[14] Dreisbach M, Leister R, Probst M, Friederich P, Stroh A and Kriegseis J 2022 Particle detection by means of neural networks and synthetic training data refinement in defocusing particle tracking velocimetry *Meas. Sci. Technol.* **33** 124001
[15] Sax C, Dreisbach M, Leister R and Kriegseis J 2023 Deep learning and hybrid approach for particle detection in defocusing particle tracking velocimetry *Meas. Sci. Technol.* **34** 095909
[16] Mehdizadeh Youshanlouei M and Rossi M 2024 Deep learning and defocus imaging for determination of three-dimensional position and orientation of microscopic objects *Phys. Fluids* **36** 082006
[17] Glover A R, Skippon S M and Boyle R D 1995 Interferometric laser imaging for droplet sizing: a method for droplet-size measurement in sparse spray systems *Appl. Opt.* **34** 8409–21
[18] Kawaguchi T, Akasaka Y and Maeda M 2002 Size measurements of droplets and bubbles by advanced interferometric laser imaging technique *Meas. Sci. Technol.* **13** 308
[19] Qieni L, Wenhua J, Tong L, Xiang W and Yimo Z 2014 High-accuracy particle sizing by interferometric particle imaging *Opt. Commun.* **312** 312–8
[20] Shen H, Saengkaew S, Gréhan G, Coetmellec S and Brunel M 2014 Interferometric out-of-focus imaging for the 3D tracking of spherical bubbles in a cylindrical channel *Opt. Commun.* **320** 156
[21] Wen B, wu Y, Zhuo Z and Wu X 2021 Characterization and verification of astigmatic interferometric particle imaging for volumetric droplet 3D position and size measurement *Adv. Powder Technol.* **32** 3476–83
[22] Maeda M, Kawaguchi T and Hishida K 2000 Novel interferometric measurement of size and velocity distributions of spherical particles in fluid flows *Meas. Sci. Technol.* **11** L13–L18
[23] Sax C, Dreisbach M and Kriegseis J 2025 Generalized approach for single-optical-access interferometric particle imaging *Phys. Rev. Appl.* **24** 044083
[24] Gire J, Denis L, Fournier C, Thiébaut E, Soulez F and Ducottet C 2008 Digital holography of particles: benefits of the 'inverse problem' approach *Meas. Sci. Technol.* **19** 074005
[25] Soulez F, Denis L, Fournier C, Thiébaut E and Goepfert C 2007 Inverse-problem approach for particle digital holography: accurate location based on local optimization *J. Opt. Soc. Am. A* **24** 1164–71
[26] Martin G, Castrejon-Pita R and Hutchings I 2011 Holographic measurement of drop-on-demand drops in flight *Int. Conf. on Digital Printing Technologies* vol 27 (https://doi.org/10.2352/.2011.27.1.art00055_2)
[27] Shen H, Coëtmellec S, Gréhan G and Brunel M 2012 Interferometric laser imaging for droplet sizing revisited: elaboration of transfer matrix models for the description of complete systems *Appl. Opt.* **51** 5357–68
[28] van de Hulst H C and Twersky V 1957 1958 light scattering by small particles: volume 10 *Wiley Series in Pure and Applied Optics* (Wiley)
[29] van de Hulst H C and Wang R T 1991 Glare points *Appl. Opt.* **30** 4755–63
[30] Dehaeck S and van Beeck J 2008 Multifrequency interferometric particle imaging for gas bubble sizing *Exp. Fluids* **45** 823–31
[31] Brouwer W 1964 Matrix methods in optical instrument design *Lecture Notes and Supplements in Physics* (W.A. Benjamin)
[32] Gerrard A and Burch J M 1975 *Introduction to Matrix Methods in Optics A Wiley-Interscience Publication* (Wiley)
[33] Leister R, Brümmer A and Kriegseis J 2022 Laser-optical shear-flow analysis across the annular gap of a simplified displacement compressor model *IOP Conf. Ser.: Mater. Sci. Eng.* **1267** 012003
[34] Olsen M G and Adrian R J 2000 Out-of-focus effects on particle image visibility and correlation in microscopic particle image velocimetry *Exp. Fluids* **29** 166–74
[35] Debye P 1908 Das elektromagnetische feld um einen zylinder und die theorie des regenbogens *Phys. Z.* **9** 1072–9
[36] Gouesbet G 2003 Debye series formulation for generalized lorenz-mie theory with the Bromwich method *Part. Part. Syst. Charact.* **20** 382–6
[37] Shen J and Wang H 2010 Calculation of Debye series expansion of light scattering *Appl. Opt.* **49** 2422–8
[38] Lentz W 1976 Generating Bessel functions in mie scattering calculations using continued fractions *Appl. Opt.* **15** 668–71
[39] Matzler C 2002 Matlab functions for mie scattering and absorption Institute of Applied Physics, University of Bern (available at: https://omlc.org/software/mie/maetzlermie/Maetzler2002.pdf)
[40] Laven P M 2024 (available at: http://philiplaven.com/mieplot.htm) (Accessed 15 October 2024)
[41] Collins S A 1970 Lens-system diffraction integral written in terms of matrix optics *J. Opt. Soc. Am.* **60** 1168–77
[42] Baues P 1969 Huygens' principle in inhomogeneous, isotropic media and a general integral equation applicable to optical resonators *Opto-Electron.* **1** 37–44
[43] Wen J and Breazeale M 1987 Gaussian beam functions as a base function set for acoustical field calculations *IEEE 1987 Ultrasonics Symp.* pp 1137–40
[44] Wen J J and Breazeale M A 1988 A diffraction beam field expressed as the superposition of Gaussian beams *J. Acoust. Soc. Am.* **83** 1752–6
[45] Bocanegra E H, Dam N, van der Voort D, Bertens G and van de Water W 2015 Measuring droplet size distributions from overlapping interferometric particle images *Rev. Sci. Instrum.* **86** 023709
[46] Ebert E, Kleinwächter A, Kostbade R and Damaschke N A 2014 Interferometric particle imaging for cavitation nuclei characterization in cavitation tunnels and in the wake flow *Proc. 17th Int. Symp. on Application of Laser Techniques to Fluid Mechanics (Lisbon, Portugal)*
[47] Karmarkar N 1984 A new polynomial-time algorithm for linear programming-II *Combinatorica* **4** 373–95
[48] Byrd R H, Gilbert J C and Nocedal J 2000 A trust region method based on interior point techniques for nonlinear programming *Math. Program.* **89** 149–85
[49] Wang Z, Bovik A, Sheikh H and Simoncelli E 2004 Image quality assessment: from error visibility to structural similarity *IEEE Trans. Image Process.* **13** 600–12

[50] Rossi M and Barnkob R 2020 A fast and robust algorithm for general defocusing particle tracking *Meas. Sci. Technol.* **32** 014001
[51] Atherton T and Kerbyson D 1999 Size invariant circle detection *Image Vis. Comput.* **17** 795–803
[52] Ratz M, Sachs S, König J and Cierpka C 2023 A deep neural network architecture for reliable 3d position and size determination for Lagrangian particle tracking using a single camera *Meas. Sci. Technol.* **34** 105203
[53] Zhang X, Dong Z, Wang H, Sha X, Wang W, Su X, Hu Z and Yang S 2023 3d positioning and autofocus of the particle field based on the depth-from-defocus method and the deep networks *Mach. Learn.: Sci. Technol.* **4** 025030
[54] Barnkob R and Rossi M 2020 General defocusing particle tracking: fundamentals and uncertainty assessment *Exp. Fluids* **61** 110
[55] Shen H, Coetmellec S and Brunel M 2013 Simultaneous 3d location and size measurement of spherical bubbles using cylindrical interferometric out-of-focus imaging *J. Quant. Spectrosc. Radiat. Transfer* **131** 153–9
[56] Brunel M, Coetmellec S, Gréhan G and Shen H 2014 Interferometric out-of-focus imaging simulator for irregular rough particles *J. Eur. Opt. Soc. -Rapid Pub.* **9** 14008
[57] Sun J, Zhang H, Wang X, Jia D, Liu T and Zhai M 2018 Determination of the orientation of transparent spheroids using interference technology *Opt. Express* **26** 14097–107
[58] Sun J, Zhang H, Fan W and Chen S 2021 Comparison of aspect ratios of ellipsoidal particles through interferometric out-of-focus images *J. Opt. Soc. Am. A* **38** 395–400